Exploring the formation pathways of formamide. Near young O-type stars

V. Allen, F. F. S. van der Tak, A. López-Sepulcre, Á. Sánchez-Monge, V. M. Rivilla, R. Cesaroni

**Astronomy
&
Astrophysics**

Exploring the formation pathways of formamide

Near young O-type stars[*]

V. Allen[1,2,3], F. F. S. van der Tak[2,3], A. López-Sepulcre[4,5], Á. Sánchez-Monge[6], V. M. Rivilla[7], and R. Cesaroni[7]

[1] NASA Goddard Space Flight Center, 8800 Greenbelt Road, Greenbelt, MD 20771, USA
e-mail: veronica.a.allen@nasa.gov
[2] Kapteyn Astronomical Institute, University of Groningen, Landleven 12, 9747 AD Groningen, The Netherlands
[3] SRON, Landleven 12, 9747 AD Groningen, The Netherlands
[4] CNRS, IPAG, Univ. Grenoble Alpes, 38000 Grenoble, France
[5] IRAM, 300 rue de la Piscine, 38406 Saint-Martin d'Hères, France
[6] I. Physikalisches Institut, Universität zu Köln, Zülpicher Straße 77, 50937 Köln, Germany
[7] INAF, Osservatorio Astrofisico di Arcetri, Largo Enrico Fermi 5, 50125 Florence, Italy

ABSTRACT

Context. As a building block for amino acids, formamide (NH_2CHO) is an important molecule in astrobiology and astrochemistry, but its formation path in the interstellar medium is not understood well.
Aims. We aim to find empirical evidence to support the chemical relationships of formamide to HNCO and H_2CO.
Methods. We examine high angular resolution ($\sim 0.2''$) Atacama Large Millimeter/submillimeter Array maps of six sources in three high-mass star-forming regions and compare the spatial extent, integrated emission peak position, and velocity structure of HNCO and H_2CO line emission with that of NH_2CHO by using moment maps. Through spectral modeling, we compare the abundances of these three species.
Results. In these sources, the emission peak separation and velocity dispersion of formamide emission is most often similar to HNCO emission, while the velocity structure is generally just as similar to H_2CO and HNCO (within errors). From the spectral modeling, we see that the abundances between all three of our focus species are correlated, and the relationship between NH_2CHO and HNCO reproduces the previously demonstrated abundance relationship.
Conclusions. In this first interferometric study, which compares two potential parent species to NH_2CHO, we find that all moment maps for HNCO are more similar to NH_2CHO than H_2CO in one of our six sources (G24 A1). For the other five sources, the relationship between NH_2CHO, HNCO, and H_2CO is unclear as the different moment maps for each source are not consistently more similar to one species as opposed to the other.

Key words. stars: massive – astrochemistry – submillimeter: ISM – ISM: general – ISM: molecules

1. Introduction

Formamide (NH_2CHO) is an important molecule to study for astrochemistry and astrobiology because its structure and content make it a likely precursor for glycine (NH_2CH_2COOH), the simplest amino acid and an important building block in the synthesis of prebiotic compounds. Saladino et al. (2012) argue that NH_2CHO may have played a key role in creating and sustaining life on the young Earth since it can lead to diversity in biologically relevant chemistry involving amino acids, nucleic acids, and sugars.

In recent years, two routes to forming NH_2CHO, which use common interstellar species, have been studied in depth. NH_2CHO forms either on dust grain ice mantles from the hydrogenation of isocyanic acid (HNCO) in the following reaction: $HNCO + H + H \rightarrow NH_2CHO$ (Charnley 1997). Subsequently, it sublimates into the gas, where we see it in hot cores and hot corinos. The alternative is from reactions between H_2CO and NH_2 in warm gas ($H_2CO + NH_2 \rightarrow NH_2CHO + H$)

(Kahane et al. 2013). It is important to note that NH_2 is especially abundant in photon-dominated regions. Other formation pathways have been tested in the lab (Jones et al. 2011; Fedoseev et al. 2016; Skouteris et al. 2017), but we do not investigate them here as the species involved fall outside the frequency range of our dataset. Laboratory studies on these reactions show that both HNCO and H_2CO can have a chemical relationship with NH_2CHO. An early study by Raunier et al. (2004) found that vacuum ultraviolet irradiation of pure HNCO ice resulted in NH_2CHO as a product. Recent laboratory work by Kaňuchová et al. (2017) shows that sufficient amounts of NH_2CHO can form in cosmic-ray-irradiated ices but the HNCO/NH_2CHO ratio does not match observations. The laboratory study by Noble et al. (2015) finds that hydrogenation of HNCO by deuterium bombardment does not lead to NH_2CHO in detectable quantities, while Barone et al. (2015) find that the H_2CO+NH_2 reaction can reproduce the abundance of NH_2CHO in IRAS16293-2422, a Sun-like protostar. Recent work by Quénard et al. (2018), which models the formation of HNCO and NH_2CHO and other peptide-bearing molecules with the N–C = O group, shows a correlation between the abundances of H_2CO and NH_2CHO as well as between HNCO and NH_2CHO without using hydrogenation.

The chemical pathway studied in Fedoseev et al. (2016) indicates that NH$_2$ may be a key precursor to both HNCO and NH$_2$CHO, indicating that they are chemically related, but not in a reactant-product relationship. Recently, further theoretical formation pathways have been investigated through quantum chemical calculations by Darla & Sitha (2019) (NH$_3$ + CO or NH$_3$ + CO$^+$) and chemical kinetics by Vichietti et al. (2019) (H$_2$O + HCN), but we do not explore those species here.

Observational evidence has been found for both chemical relationships. A tight empirical correlation has been observed using single dish observations between the abundances of HNCO and NH$_2$CHO which spans several orders of magnitude in molecular abundance (Bisschop et al. 2007; López-Sepulcre et al. 2015; Mendoza et al. 2014). This correlation between the abundances of these species is nearly linear, suggesting that the two molecules are chemically related. Atacama Large Millimeter/submillimeter Array (ALMA) observations by Coutens et al. (2016) of IRAS 16293-2422 show that the deuterium fractions in HNCO and NH$_2$CHO are very similar, implying a chemical link. On the other hand, Codella et al. (2017) observed a shock near L1157-B1 using interferometric observations. Through these observations and follow-up chemical modeling, they concluded that NH$_2$CHO is made efficiently in the gas phase from H$_2$CO, at least in this source. The possibility exists that different types of sources (shocked regions, outflow cavities, accretion disks, protostellar envelopes, etc.) may have different dominant formation routes, but this possibility stands to be examined. A comprehensive review of all research into the formation of interstellar formamide can be found in López-Sepulcre et al. (2019).

To make progress in the interpretation of the chemical link between these species, interferometric observations around a variety of sources are needed. We previously used ALMA to study emission extent, peaks, and velocity structure between HNCO and NH$_2$CHO in G35.20-0.74N (Allen et al. 2017). In the Keplerian disk candidate G35.20-0.74N B, we found that the morphology and velocity structure of HNCO and NH$_2$CHO are almost identical, and the first moment velocity differs by less than 0.5 km s^{-1}. While this suggests that HNCO has a relationship to NH$_2$CHO in this source, we could not determine a relationship with H$_2$CO because those observations did not contain spectral windows with H$_2$CO lines for comparison.

In this paper, we investigate the chemical relationships between HNCO, H$_2$CO and NH$_2$CHO using high-angular resolution ($\sim$0.2$''$ beam) ALMA observations to compare the emission morphology (Sect. 3.1), velocity structure (Sect. 3.2), and velocity dispersion (Sect. 3.3) of HNCO, H$_2$CO, and NH$_2$CHO emission in three high-mass star-forming regions (described in Sect. 2.1). To complement these observations, we use LTE spectral modeling to determine the column density, excitation temperature, average line width, and central velocity for each of these species in all the sources (Sect. 3.4). We discuss the results in Sect. 4 and summarize the main findings in Sect. 5.

2. Observations and method

2.1. Source sample

We observed three high-mass star forming regions with a high luminosity ($L_{bol} = 1-2 \times 10^5 \ L_{\odot}$). Our sources (shown in Fig. 1) are a subset of the sample studied and presented in Cesaroni et al. (2017) selected for their potential as O-type (proto)stars harboring circumstellar disks. G17.64+0.16 (hereafter G17, also known
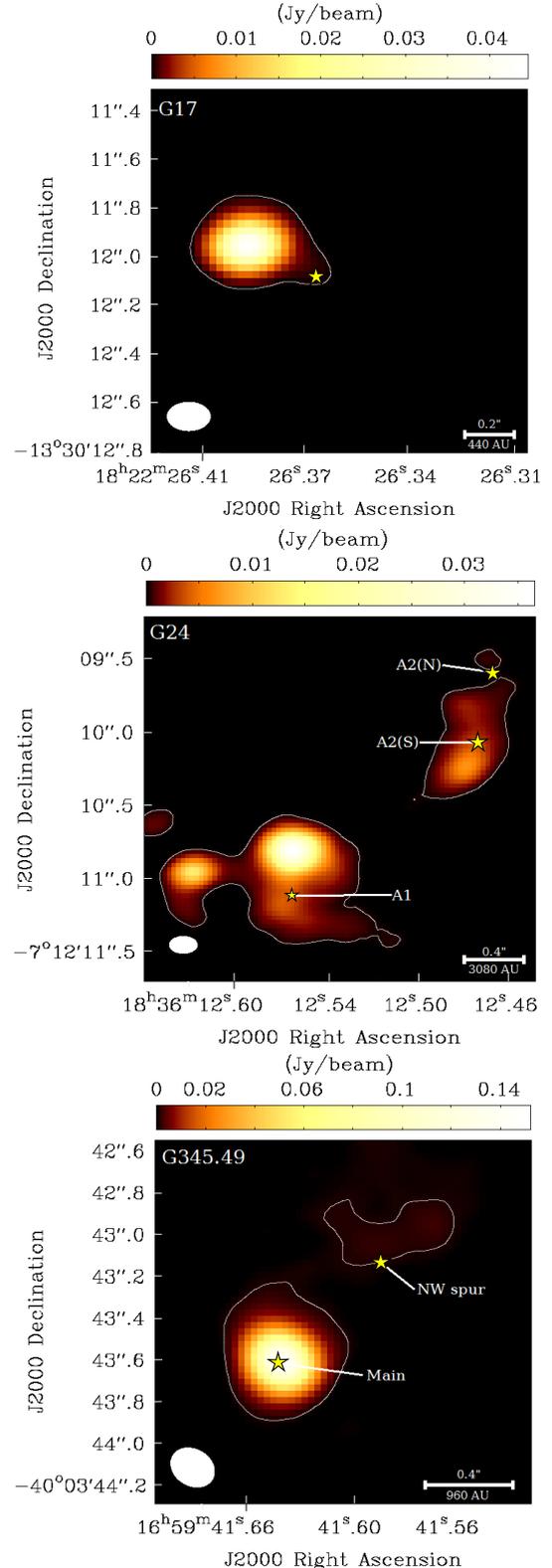

Fig. 1. Images of the 218 GHz continuum emission from Cycle 2 ALMA observations of our three regions focusing on the regions where NH$_2$CHO emission is observed. The color scale indicates the continuum flux as detailed in the color bar above each map. The white contour shows the 5σ contour levels for each panel: 1.5, 2.5, and 2.5 mJy beam^{-1}. The stars mark each of the spectral extraction points (coinciding with the zeroth moment peaks of NH$_2$CHO emission) and subsources are labeled.

as AFGL 2136 and IRAS 18196-1331), shown in the top panel of Fig. 1, is located at a distance of 2.2 kpc, has a bolometric luminosity of $1 \times 10^5 L_\odot$ and has been well studied from the infrared to the radio. G17 harbors a millimeter continuum source that is cospatial with weak H30α emission and a molecular plume to the west of the continuum source (Maud et al. 2018). G24.78+0.08 (hereafter G24), which is shown in the middle panel of Fig. 1, is located at a distance of 6.7 kpc (Reid et al. 2019), determined by trigonametric parallax, and has a bolometric luminosity of $1.7 \times 10^5 L_\odot$. There are several sources associated with this star-forming region but we focus on the hot molecular cores A1 and A2. G24 A1 contains a hypercompact HII region ($\sim$1000 au) which has been determined to be expanding through methanol, water maser, and recombination line observations (Beltrán et al. 2007; Moscadelli et al. 2018). G345.49+1.47 (hereafter G345, also known as IRAS 16562-3959), shown in the bottom panel of Fig. 1, is located at a distance of 2.4 kpc with a bolometric luminosity of $1.5 \times 10^5 L_\odot$. G345 has a continuum source associated with strong H30α emission (G345 Main) and a chemically rich region to the northwest of this continuum source (G345 NW spur) (Johnston et al., in prep.). The other three sources from the dataset described in Cesaroni et al. (2017) could not be used in these investigations because the formamide lines were strongly blended with other species.

2.2. Observations

The sources were observed with ALMA in Cycle 2 in July and September 2015 (2013.1.00489.S) in Band 6 with baselines from 40 to 1500 m. The observed frequency range was between 216.9 and 236.5 GHz divided into 13 spectral windows. The flux calibrators were Titan and Ceres and the phase calibrators were J1733-1304 (for G17 and G24) and J1709-3525 (for G345). The rms noise of the continuum maps ranges between 0.2 and 1.0 mJy beam^{-1}. The calibration and imaging were carried out using CASA[1]. A statistical method (Sánchez-Monge et al. 2018) was used within the Python-based tool STATCONT[2] for continuum subtraction as there were very few line free channels. The angular resolution is about 0.2″ and the spectral resolution in most spectral windows is 488.3 kHz, but higher (244.1 kHz) from 220.30 to 220.767 GHz and lower (1953.1 kHz) in the spectral window from $\sim$216.976 to 218.849 GHz. The bandwidths for all spectral windows are <2 GHz with the largest being 1.8 GHz. For full details on observations and continuum subtraction see Cesaroni et al. (2017). The continuum intensity for subsources showing H30α emission were corrected for free-free emission with direct measurements for G17 from Maud et al. (2018), G24 A1 from Moscadelli et al. (2018), and calculated for G345 using the spectral index fit from Guzmán et al. (2016).

2.3. Line identification

Spectra were extracted from the positions indicated with a star in Fig. 1 corresponding with the peak(s) of NH$_2$CHO emission (positions listed in Table 2) from the continuum subtracted images of each sub-source (except G345 Main) using CASA. We investigate if the NH$_2$CHO transitions are blended by performing simultaneous fits of the species NH$_2$CHO, HNCO, H$_2$CO, and species that were potentially blended with NH$_2$CHO (C$_2$H$_5$OH,

---

[1] Common Astronomy Software Applications is available from http://casa.nrao.edu/
[2] STATCONT is freely accessible here: https://hera.ph1.uni-koeln.de/~sanchez/statcont

---

Table 1. Source properties.

Source	v_{LSR} (km s^{-1})	Distance (kpc)	L_{bol} ($10^5 L_\odot$)
G17.64+0.16	22.5	2.2	1.0
G24.78+0.08	111.0	6.7	1.7
G345.49+1.47	−12.6	2.4	1.5

Notes. Distance and luminosity values from the rms database (Lumsden et al. 2013) (The Red MSX Source survey database at http://rms.leeds.ac.uk/cgi-bin/public/RMS_DATABASE.cgi, which was constructed with support from the Science and Technology Facilities Council of the UK) except distance and L_{bol} for G24.78+0.08 which is from Reid et al. (2019).

Table 2. Spectral extraction points for line identification and spectral modeling with XCLASS (Sect. 3.4).

Source	RA (J2000)	Dec (J2000)	N_{core} (cm^{-2})	H30α
G17	18:22:26.370	−13:30:12.06	1.0×10^{25}	✓
G24 A1	18:36:12.544	−07:12:11.14	1.3×10^{24}	✓
G24 A2(N)	18:36:12.465	−07:12:09.61	9.9×10^{23}	
G24 A2(S)	18:36:12.471	−07:12:10.09	8.2×10^{23}	
G345 Main	16:59:41.628	−40:03:43.63	9.8×10^{25}	✓
G345 NW spur	16:59:41.586	−40:03:43.15	2.3×10^{25}	

Notes. These points coincide with the NH$_2$CHO peak used for each source. N_{core} was determined as in Sánchez-Monge et al. (2014) using the continuum intensity at the spectral extraction point assuming a T_{dust} of 100 K, a dust opacity of 1.0 cm^2 g^{-1} (Ossenkopf & Henning 1994), and a gas-to-dust ratio of 100. Check mark (✓) symbols indicate the detection of H30α emission toward the sub-source. For these sources, the continuum was corrected for free–free emission.

CH$_3$CN ($v_8 = 1$), and CH$_3^{18}$OH) via the XCLASS[3] software (Möller et al. 2017) assuming local thermal equilibrium (LTE). This software models the data by solving the radiative transfer equation for an isothermal object in one dimension, taking into account source size and opacity. The observed spectra and the XCLASS fits are shown in Appendix B. Using this software, we determine the excitation temperature (T_{ex}), column density (N_{col}), line width (FWHM), and velocity offset (v_{LSR}) for each modeled species (see details in Sect. 3.4). The model parameters FWHM and v_{LSR} were constrained using Gaussian fits of the observed transitions and allowed to vary ±0.5 km s^{-1} from the measured central velocity. The T_{ex} free parameter was allowed to vary between 50 and 300 K for HNCO and NH$_2$CHO and between 70 and 400 K for H$_2$CO. The temperature of H$_2$CO was modeled using higher temperatures and a source size smaller than the beam size ($\sim$0.15″) in order to fit the emission originating on the small scale. The range explored for N_{col} for each source is equivalent to abundances between 10^{-13} and 10^{-5}. Because G345 Main shows very strong continuum emission ($T_B \sim 90$ K) and absorption features, we used spectra extracted from non-continuum subtracted images and also modeled the continuum level within XCLASS.

In general, we compare transitions with similar E_{up} values (60–100 K) except where we consider HNCO (3) which has an E_{up} of 432.9 K. Additionally, where one species can have strong emission due to larger abundances, another can be undetected

---

[3] Available from: https://xclass.astro.uni-koeln.de/

Table 3. Transition properties from the Cologne Database for Molecular Spectroscopy (CDMS) (Endres et al. 2016).

Species	Transition	Frequency (MHz)	E_{up} (K)	A_{ij} (s^{-1})	Sources
HNCO (1)	$10_{0,10}$–$9_{0,9}$	219 798.27	58.0	1.47×10^{-4}	G24
HNCO (2)	$10_{1,9}$–$9_{1,8}$	220 584.75	101.5	1.45×10^{-4}	G17, G345
HNCO (3)	$10_{3,7}$–$9_{3,6}$	219 656.77	432.9	1.20×10^{-4}	G24, G345
NH$_2$CHO (1)	$10_{1,9}$–$9_{1,8}$	218 459.21	60.8	7.47×10^{-4}	G17, G345
NH$_2$CHO (2)	$11_{2,10}$–$10_{2,9}$	232 273.64	78.9	8.81×10^{-4}	G24
H$_2$CO (1)	$3_{0,3}$–$2_{0,2}$	218 222.19	20.9	2.82×10^{-4}	G17, G24, G345
H$_2$CO (2)	$3_{2,2}$–$2_{2,1}$	218 475.63	68.1	1.57×10^{-4}	G17, G24, G345
H$_2$CO (3)	$3_{2,1}$–$2_{2,0}$	218 760.07	68.1	1.58×10^{-4}	G17, G24, G345

Notes. The last column shows the sources in which this transition appeared. HNCO (3) has a much higher upper energy level than the other transitions, so we consider it cautiously. The CDMS catalog can be accessed here: `https://cdms.astro.uni-koeln.de/`
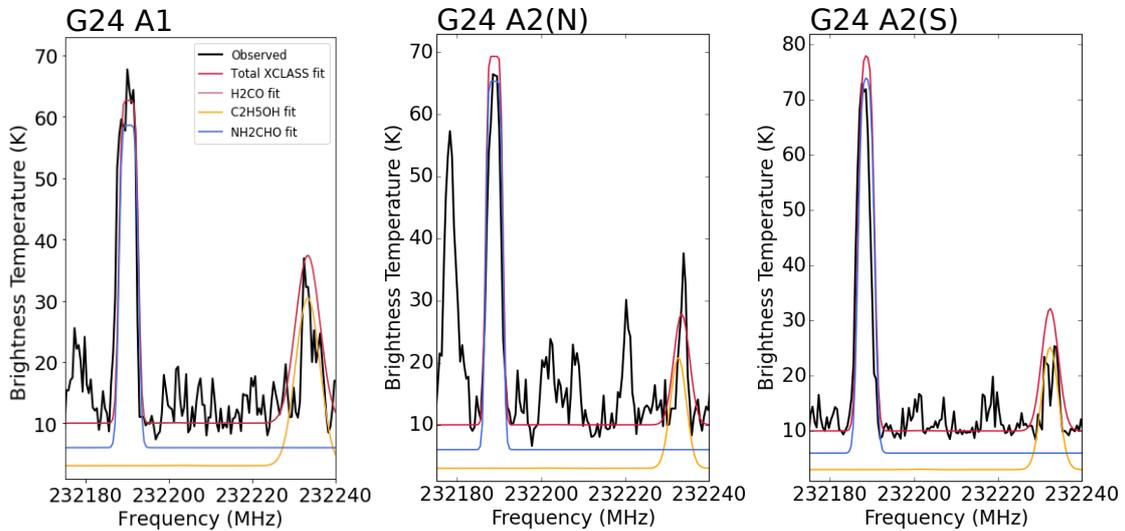

Fig. 2. Observed and synthetic spectra of G24 A1 (*left*), A2(N) (*middle*), and A2(S) (*right*) with fits showing NH$_2$CHO (2) (dark blue). The continuum levels are offset for easy viewing.

because the telescope is not sensitive enough to detect a much weaker signal. The transitions used in the analysis in this work are listed in Table 3. There were two different unblended transitions of NH$_2$CHO used: NH$_2$CHO (1) used for G17 and G345 and NH$_2$CHO (2) for G24. NH$_2$CHO (2) (defined in Table 3) is the best transition as it is unlikely to be blended (see the best fit spectra in Fig. 2) but it only appears within the spectral windows of G24 due to its high v_{LSR} (Table 1). The transitions identified for HNCO and H$_2$CO are generally unblended, but the NH$_2$CHO (1) emission is potentially blended with ethanol (C$_2$H$_5$OH) in G345 (Fig. 3). In G17, C$_2$H$_5$OH is not detected, so NH$_2$CHO (1) is considered to be unblended. For NH$_2$CHO (1) in G345, we compare the C$_2$H$_5$OH transition that can produce a blend with NH$_2$CHO (at 218 461.23 MHz) with a similar transition with the same upper energy level, E_{up}, (23.9 K) and almost the same Einstein coefficient, A_{ij}, (6.54×10^{-5} vs. 6.60×10^{-5} s^{-1}) at 217 803.69 MHz. We use the NH$_2$CHO (1) transition for G345 for three reasons: the emission in G345 from the isolated C$_2$H$_5$OH transition at 217 803.69 MHz is much weaker than the line that is blended with NH$_2$CHO (1), the peak integrated emission of NH$_2$CHO (1) is ~8 times stronger than that of C$_2$H$_5$OH (0.24 vs. 0.03 Jy beam^{-1} km s^{-1}), and the two have completely different morphology (see Fig. A.1).

3. Comparison of formamide emission to possible chemically-related species

In this section, we derive gas properties empirically from moment maps. From the integrated intensity maps (zeroth moment), we locate the peak of line emission to high accuracy with a 2D-Gaussian fit accuracy to 0.01″. We assume, then, that if two species peak in the same location, and have the same velocity and line width, then they are in the same gas and are therefore related (either they have been released from the ice around the same time or they have formed in the same gas). From the velocity maps (first moment), we measure the average central velocity for each transition at each pixel and subtract these values from each other. A small difference between these velocities for different species suggests that they are in the same gas as they are moving in the same manner. Peak positions and average velocities can be affected by optical depth, especially when dealing with the main isotope of a species (i.e. not isotopologues). Using RADEX (van der Tak et al. 2007), a one dimensional non-LTE radiative transfer code, we have determined that the optical depths for the H$_2$CO lines range from 33 to 430 while those for HNCO lines are much lower ranging from 0.4 to 69. The last quantity we derive from moment maps is the velocity dispersion
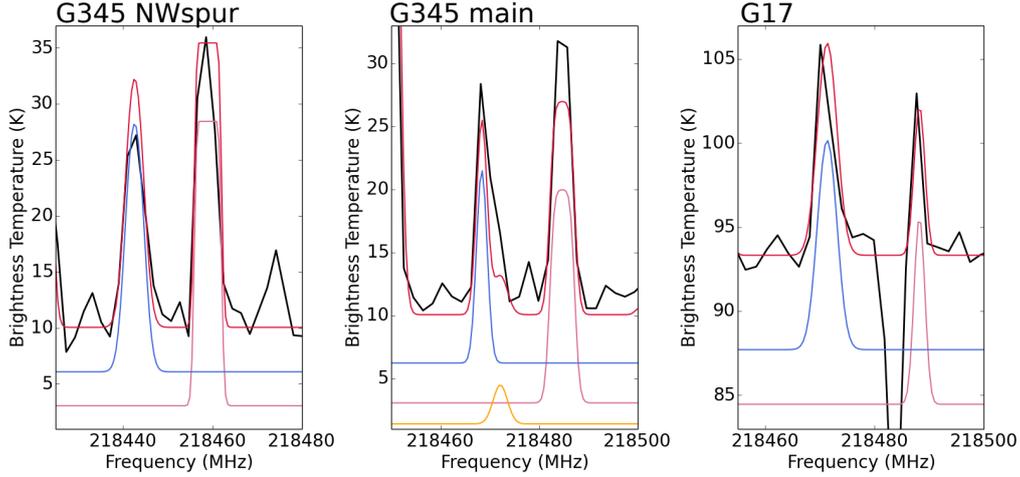
Fig. 3. Spectra with fits showing NH₂CHO (1) toward G345 NW spur (*left*), G345 Main (*middle*) and G17 (*right*). NH₂CHO (1) is weakly blended with C₂H₅OH in the spectra of G345 NW spur but unblended in G345 Main. The continuum levels are offset for easy viewing.
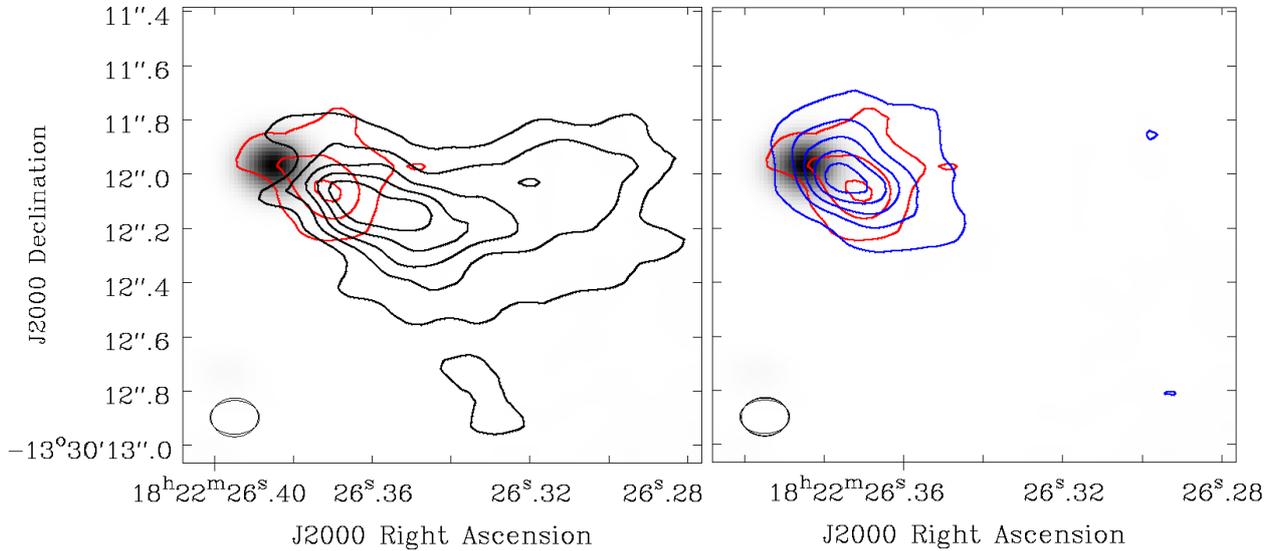

Fig. 4. G17 zeroth moment maps (contours) overlaid on the dust continuum (grayscale). *Left*: the black contours show the H₂CO (2) transition ($E_{up} = 68.1$ K) from 5σ to a peak of 0.175 Jy beam⁻¹ km s⁻¹ (contour levels 0.021, 0.052, 0.083, 0.113, and 0.144 Jy beam⁻¹ km s⁻¹). The red contours show NH₂CHO (1) emission (($E_{up} = 60.8$ K) from 5σ to 0.268 Jy beam⁻¹ km s⁻¹ (contour levels 0.022, 0.071, 0.120, 0.170, and 0.219 Jy beam⁻¹ km s⁻¹). *Right*: the blue contours show the extent of the HNCO (2) emission ($E_{up} = 101.5$ K) from 5σ to 0.146 Jy beam⁻¹ km s⁻¹ (contour levels 0.010, 0.037, 0.064, 0.092, and 0.119 Jy beam⁻¹ km s⁻¹) with the red contours showing NH₂CHO (as in the left frame).

(second moment) map differences. Velocity dispersion gives the average line width at each pixel which is related to the level of turbulence in the gas. A small difference between velocity dispersion values shows that the gas emitting each transition has a similar turbulence level which suggests that they are in the same gas.

3.1. Comparison of spatial distribution

3.1.1. G17

Although G17 is not associated with strong emission of typical complex organic molecules (e.g., CH₃OCHO, CH₂CHCN) (Cesaroni et al. 2017, Maud et al. 2018), it has a clear detection of NH₂CHO. We see in Fig. 4 that the integrated emission (moment zero) map of NH₂CHO is slightly more compact than that of HNCO (0.58 vs. 0.76″ or 1275 vs. 1675 au). Both species are offset from the continuum but the emission peaks of HNCO and

NH₂CHO are separated by $\sim 0.1''$ (220 au). For H₂CO, the emission is much more extended (up to 1.6″ or ~3500 au). The H₂CO (1), (2), and (3) (see Table 3 for line properties) zeroth moment peaks are separated from the NH₂CHO peak by 0.07″, 0.1″, and 0.22″ respectively. The lowest energy ($E_{up} = 20.9$ K) H₂CO (1) peak is slightly closer to the NH₂CHO peak than the HNCO peak (0.07″ vs. 0.1″).

3.1.2. G24

G24 has three subsources A1, A2(N), and A2(S). In Fig. 5 we find that the H₂CO emission in G24 is much more extended than the NH₂CHO emission. In G24 A1, the extent of the H₂CO emission is 1.71″ (~11 500 au) from northeast to southwest whereas the NH₂CHO emission extends 0.9″ (~6000 au) in the same direction. In G24 A2, the H₂CO emission extends 2.0″ (~13 400 au) whereas the NH₂CHO emission spans 1.1″
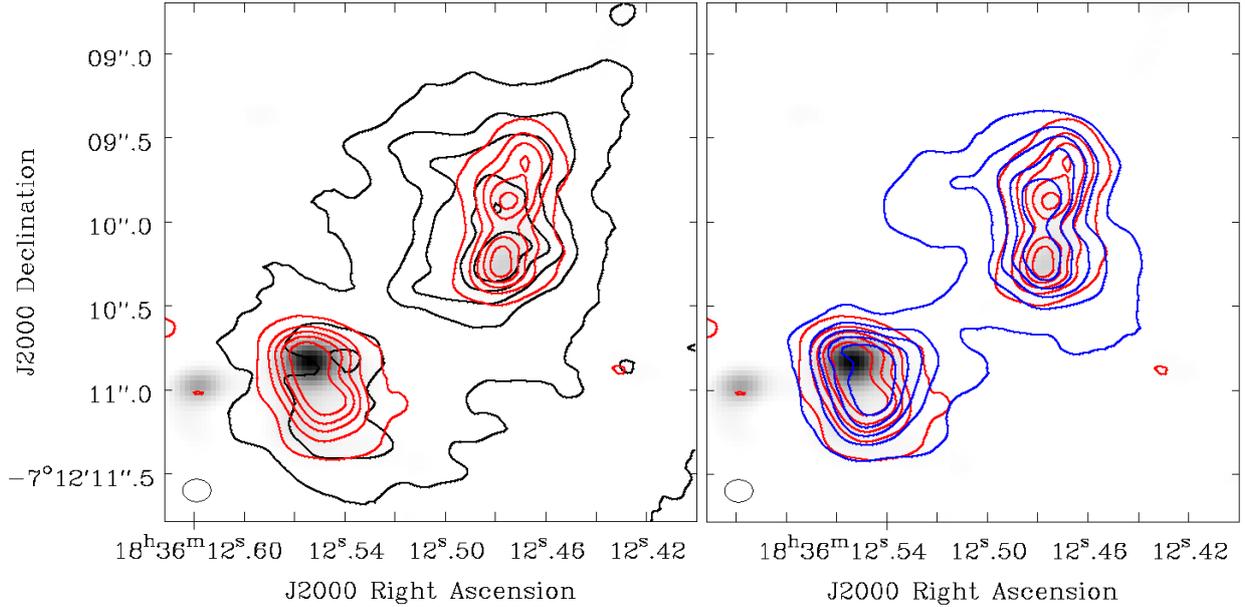
Fig. 5. G24 zeroth moment maps (contours) overlaid on the dust continuum (grayscale). *Left*: the black contours show the H_2CO (3) transition ($E_{up} = 68.1$ K) from 5σ to a peak of 0.674 Jy beam^{-1} km s^{-1} (contour levels 0.03, 0.16, 0.29, 0.42, and 0.55 Jy beam^{-1} km s^{-1}). The red contours show NH_2CHO (2) emission ($E_{up} = 78.9$ K) from 5σ to 0.512 Jy beam^{-1} km s^{-1} (contour levels 0.026, 0.123, 0.220, 0.318, and 0.415 Jy beam^{-1} km s^{-1}). *Right*: the blue contours show the extent of the HNCO (1) emission ($E_{up} = 58.0$ K) from 5σ to 0.738 Jy beam^{-1} km s^{-1} (contour levels 0.031, 0.172, 0.314, 0.455, and 0.597 Jy beam^{-1} km s^{-1}) with the red contours showing NH_2CHO (as in the left frame).
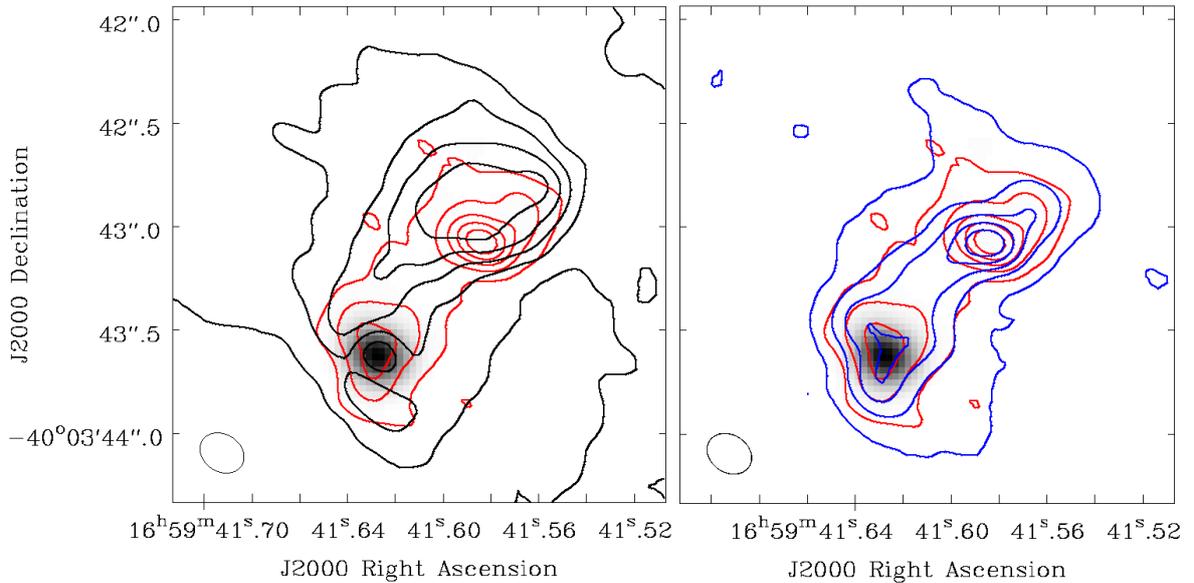
Fig. 6. G345 zeroth moment maps (contours) overlaid on the dust continuum (grayscale). *Left*: the black contours show the H_2CO (3) transition ($E_{up} = 68.1$ K) from 5σ to a peak of 0.402 Jy beam^{-1} km s^{-1} (contour levels 0.027, 0.102, 0.177, 0.232, and 0.327 Jy beam^{-1} km s^{-1}). The red contours show NH_2CHO (1) emission ($E_{up} = 60.8$ K) from 5σ to 0.242 Jy beam^{-1} km s^{-1} (contour levels 0.020, 0.064, 0.109, 0.153, and 0.198 Jy beam^{-1} km s^{-1}). *Right*: the blue contours show the extent of the HNCO (2) emission ($E_{up} = 101.5$ K) from 5σ to 0.428 Jy beam^{-1} km s^{-1} (contour levels 0.014, 0.097, 0.180, 0.262, and 0.345 Jy beam^{-1} km s^{-1}) with the red contours showing NH_2CHO (as in the left frame).

($\sim$7400 au). The extent of HNCO in these sources is 1.1$''$ ($\sim$7400 au) at G24 A1 and 1.5$''$ ($\sim$10 050 au) for G24 A2. The integrated emission for NH_2CHO and HNCO (3) breaks off between A1 (to the southeast) and A2 (to the northwest) whereas for the H_2CO transitions and HNCO (1) there is some emission between the two continuum sources. In G24 A1, the separation between all HNCO or H_2CO and NH_2CHO emission peaks are between 0.04 and 0.35$''$ (270–2350 au) and the closest peak to NH_2CHO is that of HNCO (3). In the case of G24 A1, we

must remember that optical depth effects primarily affect H_2CO in this source.

The NH_2CHO, HNCO, and H_2CO emission in G24 A2 have two significant NH_2CHO integrated intensity peaks of similar strength separated by about 0.35$''$ ($\sim$2350 au) that we refer to as A2(N) and A2(S) (positions of each peak indicated in Fig. 1). The two emission peaks in G24 A2 complicate things slightly, as it is difficult to draw boundaries between the velocity maps of the two peaks. Nevertheless we can determine the positions

of the emission peaks and analyze them separately. The more northerly H_2CO (2) peak was in between the NH_2CHO A2(N) and (S) peaks with a distance between H_2CO (2) A2(N) and NH_2CHO (2) A2(N) of 0.25″ (~1670 au) and between H_2CO (2) A2(N) and NH_2CHO (2) A2(S) of 0.18″ (~1200 au). The H_2CO (3) A2 peaks are nearer to the respective NH_2CHO peaks at 0.07″ (~470 au) from A2(N) and 0.03″ (~200 au) from A2(S). In G24 A2(N), the closest peak to the NH_2CHO is the lower energy (58 K) HNCO (1) transition. In A2(S), the HNCO (3) transition and the H_2CO (3) peaks are equally separated from NH_2CHO peak at 0.03″ (~200 au).

3.1.3. G345

The two subsources in G345 (described in Fig. 1) are G345 Main and G345 NW spur. From the spectra extracted from G345 Main, we note that the chemical composition appears to be affected by a source of strong $H30\alpha$ emission within which is ionizing the region and destroying complex molecular species, but the closest peak to the NH_2CHO peak (by far) is HNCO (2). The spectra associated with G345 NW spur show that it is a very chemically diverse region – possibly an outflow cavity associated with G345 Main. The HNCO (2) and (3) emission peaks are equally the closest to the NH_2CHO peak in G345.49 NW spur (0.03″).

Figure 6 shows that HNCO (2) and NH_2CHO (1) have similar extent and velocity structure at the Main and NW spur positions. There is little high energy HNCO (3) emission at G345 Main. The H_2CO transitions peak at the NW spur, but there is still emission at Main, without a clear peak. We take the pixel with the highest intensity on the area designated to Main despite the emission being extended across the two parts of the source. In Main, the low energy HNCO transition peaks very close to the NH_2CHO peak (0.04″ away ~100 au), but the higher energy HNCO transition and all of the H_2CO transitions peak 0.21-0.25″ from the NH_2CHO peak. In the NW spur, both HNCO transitions peak very near the NH_2CHO peak (0.03″ ~ 75 au) whereas all three H_2CO transitions are farther at 0.21–0.24″ (500–575 au).

3.1.4. Summary of spatial distribution comparison

For our six subsources in these regions (see Table 4 and Fig. 7), it is clear that the integrated emission peaks of HNCO are closer to the peaks of NH_2CHO than the H_2CO peaks. The morphology of the HNCO emission is also more similar to NH_2CHO, as the H_2CO emission tends to be much more extended and even the brightest emission (see higher intensity contours in Figs. 4–6) have a different shape to the NH_2CHO emission. The lack of NH_2CHO emission in the more extended regions indicates that it can be more efficiently made from H_2CO (in the gas phase) near the continuum peaks than farther out in these cases. It is clear from the H_2CO emission toward G24 A1 and G345 Main, that these transitions are suffering by optical depth effects.

3.2. Comparison of the velocity field

The velocity field of each molecule was investigated by creating the first order moment map for each transition listed in Table 3. These maps were then subtracted from each other to determine the difference between the gas velocities for each species. Where possible, two transitions from the same species were also compared to determine the "internal error", as the velocity difference of transitions within the same gas implies a

Table 4. Peak separations between listed transitions and NH_2CHO (in arcseconds).

Species	G17	G24 A1	G24 A2(N)	G24 A2(S)	G345 Main	G345 NW spur
HNCO (1)	N/A	0.08	0.03	0.06	N/A	N/A
HNCO (2)	0.1	N/A	N/A	N/A	0.04	0.03
HNCO (3)	N/A	0.04	0.04	0.03	0.21	0.03
H_2CO (1)	0.07	0.35	0.12	0.1	0.21	0.21
H_2CO (2)	0.1	0.29	0.25	0.06	0.25	0.24
H_2CO (3)	0.22	0.27	0.07	0.03	0.25	0.23

Notes. The error in the peak position is ~0.01″. Transitions in Col. 1 are labeled as in Table 3. For G24 A2 (N) and (S) the distances are measured from the corresponding northern or southern peaks.
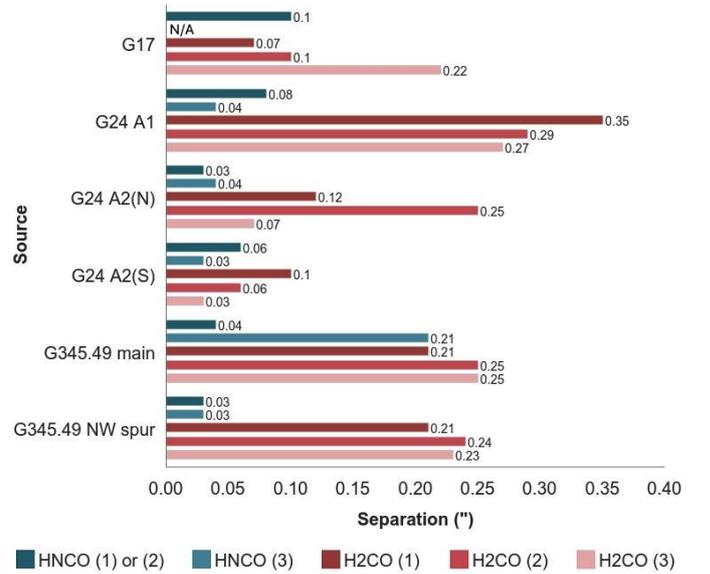

Fig. 7. Separations between NH_2CHO and each peak of HNCO and H_2CO. For the G24 sources HNCO (1) is used instead of HNCO (2) (see Table 3). The error in the peak position is ~0.01″.

lower limit for accuracy. Histograms were made for the absolute values of each velocity difference map showing the number of pixels within each bin (see Appendix C). The average value and standard deviation of these histograms were used to determine which species was most similar to NH_2CHO. Results are detailed per source below and summarized in Table 5 and Fig. 8.

3.2.1. G17

Figure 9 shows that the velocity differences between HNCO and NH_2CHO and H_2CO and NH_2CHO are not significantly different. The average velocity difference for HNCO (2) is 0.78 km s^{-1}, whereas the differences for H_2CO (2) and (3) are 0.72 and 0.67 km s^{-1}, respectively. For G17 overall the H_2CO transitions are on average more similar to NH_2CHO. HNCO (3) is not detected toward G17.

3.2.2. G24

Figure 10 shows that the range of velocity differences in G24 A2(N) and A2(S) (to the northwest) are greater between HNCO and NH_2CHO than H_2CO and NH_2CHO with the smallest average difference between H_2CO (3) and NH_2CHO for

Table 5. Average values (with the standard deviation in parentheses) of the histograms (see Appendix C) of each velocity (first moment) difference map.

Transitions	G17	G24 A1	G24 A2(N)	G24 A2(S)	G345 NW spur	G345 Main
H_2CO (2) – H_2CO (3)	0.42 (0.58)	0.27 (0.54)	0.22 (0.50)	0.34 (0.61)	0.27 (0.39)	0.43 (0.43)
HNCO (2) – HNCO (3)	N/A	0.73 (0.44)	0.74 (0.48)	0.44 (0.56)	0.25 (0.18)	N/A
H_2CO (2) – NH_2CHO	0.72 (0.54)	1.14 (1.14)	0.58 (0.46)	1.13 (1.06)	0.97 (0.90)	0.76 (0.62)
H_2CO (3) – NH_2CHO	0.67 (0.38)	1.15 (1.11)	0.53 (0.38)	1.16 (1.10)	0.91 (0.89)	0.84 (0.73)
HNCO (2) – NH_2CHO	0.78 (0.74)	1.30 (0.92)	1.45 (0.75)	1.23 (0.82)	1.18 (1.07)	0.51 (0.38)
HNCO (3) – NH_2CHO	N/A	1.01 (0.49)	0.81 (0.28)	1.26 (0.85)	0.86 (0.35)	N/A

Notes. All units are km s^{-1}. For G24, HNCO (1) is used instead of HNCO (2). G17 and G345 Main have only one HNCO transition, so the internal error for HNCO transitions cannot be determined.
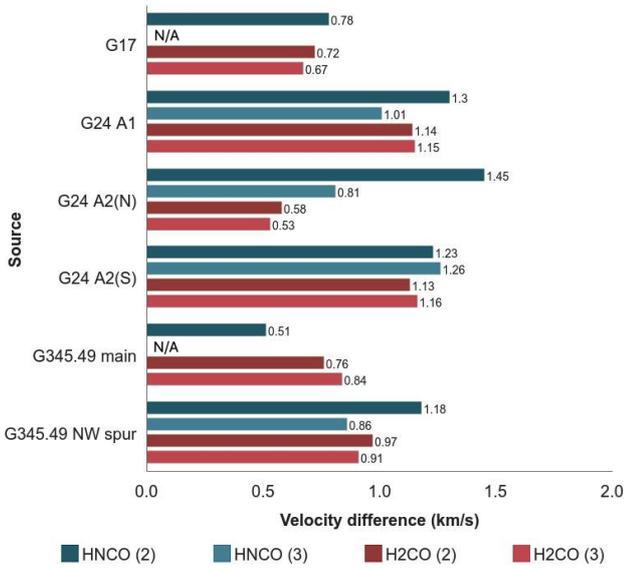
Fig. 8. Average velocity difference between NH_2CHO and transitions HNCO (2) and (3) and H_2CO (2) and (3). For the G24 sources HNCO (1) is used instead of HNCO (2) (see Table 3).

A2(N) and between H_2CO (2) and NH_2CHO for A2(S) at 0.53 and 1.13 km s^{-1}, respectively. It is less obvious visually for G24 A1 (to the southeast), but we can see from the average values listed in Table 5 that the average difference closest to zero is between HNCO (3) and NH_2CHO at 1.01 km s^{-1}.

3.2.3. G345

Figure 11 shows the velocity differences in G345 Main (to the southeast) and NW spur (to the northwest). The range of values for the velocity difference is smaller for HNCO and NH_2CHO for both subsources. The smallest average velocity difference for G345 NW spur is between HNCO (3) and NH_2CHO at 0.86 km s^{-1}, closely followed by H_2CO (3) and (2) at 0.91 and 0.97 km s^{-1}, respectively. For G345 Main, the smallest average difference is between HNCO (2) and NH_2CHO at 0.51 km s^{-1} with H_2CO (2) and (3) averages of 0.76 and 0.84 km s^{-1}. Within errors, the velocity fields of the two precursors are equally similar to that of NH_2CHO. HNCO (3) is not detected toward G345 Main.

3.2.4. Summary of the velocity field comparison

We see in the Table 5 and Fig. 8 that there are an equal number of subsources where the average velocity difference is closest to

zero for each of our related species. For a few sources, the range of average differences between different transitions is very small. For G17 in particular, the averages are 0.67, 0.72, and 0.78 km s^{-1} for H_2CO (3), H_2CO (2) and HNCO (2), respectively. For G24 A2(N) the difference is clearer with average velocity differences of 0.53, 0.58, 0.81, and 1.45 km s^{-1} for H_2CO (3), H_2CO (2), HNCO (3) and HNCO (1), respectively. In the cases of G24 A1 and G24 A2(N), the internal error for HNCO is much larger than that of H_2CO (0.73 and 0.74 vs. 0.27 and 0.22 km s^{-1}). This indicates that, in terms of errors, the difference between NH_2CHO and H_2CO is stronger than the difference between NH_2CHO and HNCO in these sources.

3.3. Comparison of the velocity dispersion

Second order moment maps were made for each of the transitions studied for each star-forming region. These maps were then subtracted from each other to determine the difference between the velocity dispersion for each species. Though it may be affected by optical depth, similar line widths between species can suggest that they are in the same gas. As in Sect. 3.2, transitions from the same species were compared to determine internal error. Histograms were made of the absolute values of each dispersion difference map showing the number of pixels within each velocity bin. The average value and standard deviation of these histograms were used to determine which species was most similar to NH_2CHO. Results are detailed per source in the text and summarized in Table 6 and Fig. 12. The histograms for this analysis are shown in Appendix C.

3.3.1. G17

Figure 13 shows the difference at each pixel between the second order moment maps of H_2CO and NH_2CHO and HNCO and NH_2CHO toward G17. It is clear that the difference between HNCO and NH_2CHO is smaller and we determine that the average difference is 0.52 km s^{-1} for HNCO (2), whereas for H_2CO (2) and (3) the average differences are 0.68 and 0.86 km s^{-1}, respectively. HNCO (3) is not detected toward G17.

3.3.2. G24

Figure 14 shows the difference at each pixel between the second order moment maps of H_2CO and NH_2CHO and HNCO and NH_2CHO toward G24 A1 (to the southeast) and G24 A2(N) and A2(S) (to the northwest). HNCO (3)-NH_2CHO has the smallest average velocity dispersion difference for all three subsources of G24 at 0.41 km s^{-1} for A1, 0.21 km s^{-1} for A2(N), and 0.47 km s^{-1} for A2(S).
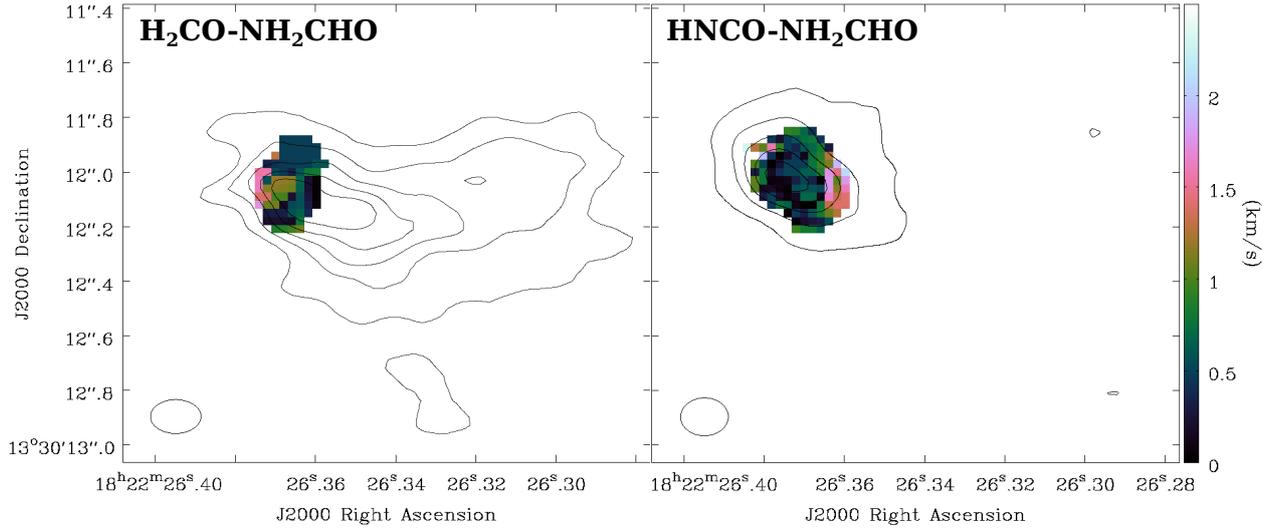
Fig. 9. Velocity difference (from first moment maps) at each pixel in G17 between (*left*) H_2CO (2) and NH_2CHO (1) and (*right*) HNCO (2) and NH_2CHO (1). The contours show the integrated intensity maps for H_2CO (2) and HNCO (2) as in Fig. 4. The velocity scale is the same for both panels.
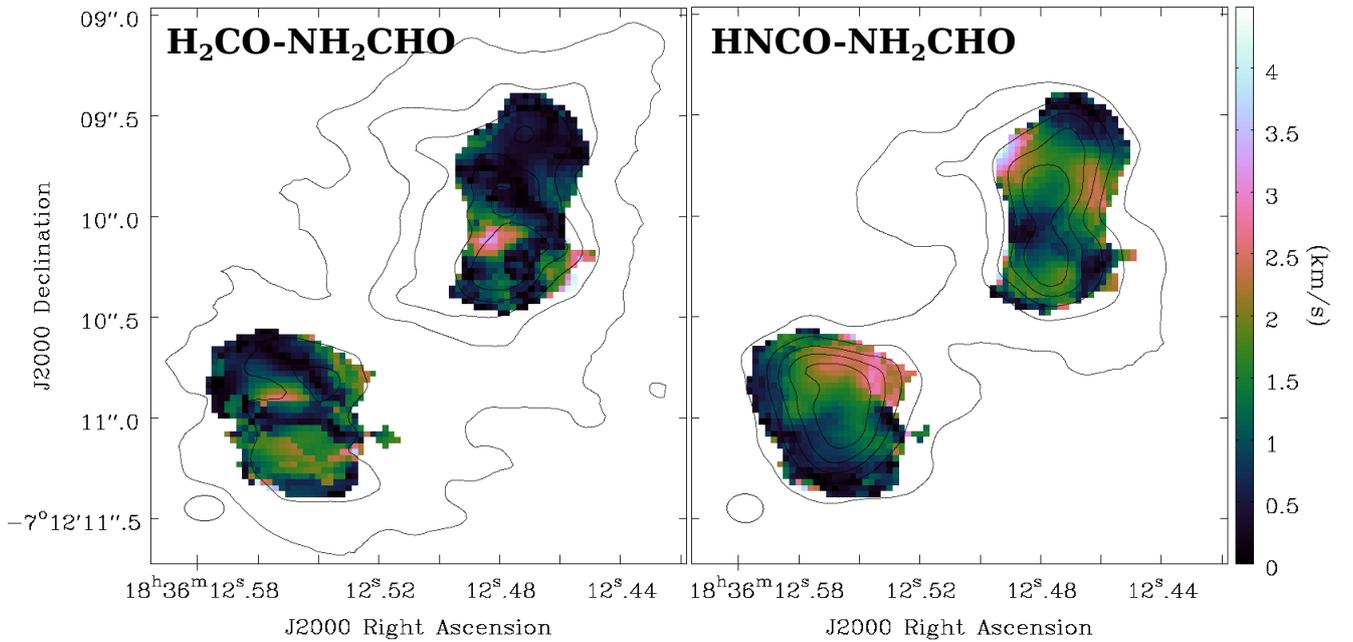

Fig. 10. Velocity difference (from first moment maps) at each pixel in G24 between (*left*) H_2CO (3) and NH_2CHO (2) and (*right*) HNCO (1) and NH_2CHO (2). The contours show the integrated intensity maps for H_2CO (3) and HNCO (1) as in Fig. 5. The velocity scale is the same for both panels.

3.3.3. G345

Figure 15 shows the difference at each pixel between the second order moment maps of H_2CO and NH_2CHO and HNCO and NH_2CHO toward G345 Main (to the southeast) and G345 NW spur (to the northwest). For G345 Main, it is clear from the figure and Table 6 that HNCO (2) has the smallest average difference between velocity dispersion values at 0.53 km s^{-1}. The average second order moment map differences for H_2CO (2) and (3) are 0.80 and 0.77 km s^{-1}, respectively, and there is no HNCO (3) emission toward G345 Main. The average difference between H_2CO (3) and NH_2CHO in G345 NW spur is smallest at 0.80 km s^{-1}, but the average difference for HNCO (2)-NH_2CHO

is 0.81 km s^{-1}, so these two maps are equally similar within errors.

3.3.4. Summary of velocity dispersion comparison

As a measure of the similarity between the motions of the gas containing each species, the line width test comes out in favor of HNCO for five out of six subsources. In the sixth (G345 NW spur), the difference between H_2CO (3)-NH_2CHO and HNCO (2)-NH_2CHO is only 0.01 km s^{-1}. In the five subsources that show the velocity dispersion of HNCO as definitively closest to NH_2CHO, the average values are also consistent with zero if we
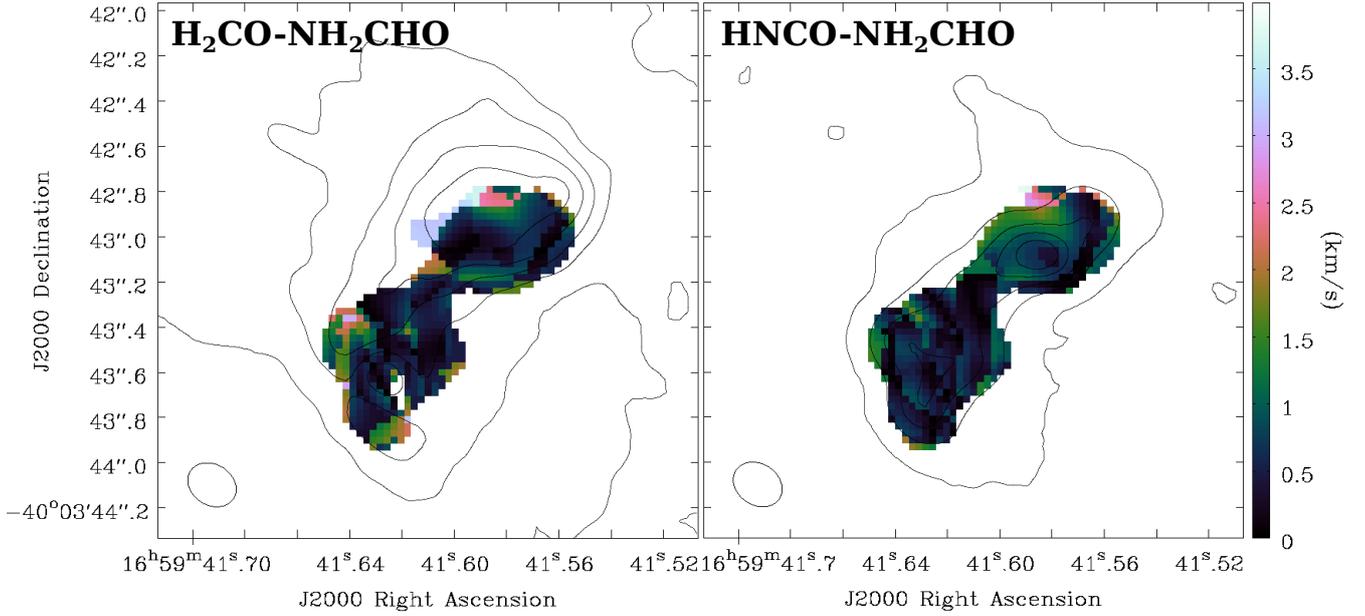
Fig. 11. Velocity difference (from first moment maps) at each pixel in G345 between (*left*) H$_2$CO (2) and NH$_2$CHO (1) and (*right*) HNCO (2) and NH$_2$CHO (1). The contours show the integrated intensity maps for H$_2$CO (2) and HNCO (2) as in Fig. 6. The velocity scale is the same for both panels.

Table 6. Average values (with the standard deviation in parentheses) of the histograms of each dispersion (second moment) difference map.

Transitions	G17	G24 A1	G24 A2(N)	G24 A2(S)	G345 NW spur	G345 Main
H$_2$CO (2) – H$_2$CO (3)	0.08 (0.60)	0.12 (0.58)	0.17 (0.61)	0.13 (0.67)	0.17 (0.58)	0.07 (0.56)
HNCO (2) – HNCO (3)	N/A	0.99 (0.53)	1.11 (0.58)	0.98 (0.67)	0.67 (0.23)	N/A
H$_2$CO (2) – NH$_2$CHO	0.68 (0.68)	0.75 (0.55)	0.79 (0.48)	1.59 (0.86)	0.92 (0.44)	0.80 (0.73)
H$_2$CO (3) – NH$_2$CHO	0.86 (0.69)	0.62 (0.51)	0.65 (0.47)	1.63 (0.91)	0.80 (0.50)	0.77 (0.70)
HNCO (2) – NH$_2$CHO	0.52 (0.39)	0.67 (0.62)	0.95 (0.59)	0.81 (0.68)	0.81 (0.41)	0.53 (0.45)
HNCO (3) – NH$_2$CHO	N/A	0.41 (0.41)	0.21 (0.19)	0.47 (0.47)	1.32 (0.49)	N/A

Notes. All units are km s^{-1}. For G24, HNCO (1) is used instead of HNCO (2). G17 and G345 Main have only one HNCO transition, so the internal error for HNCO transitions cannot be determined.
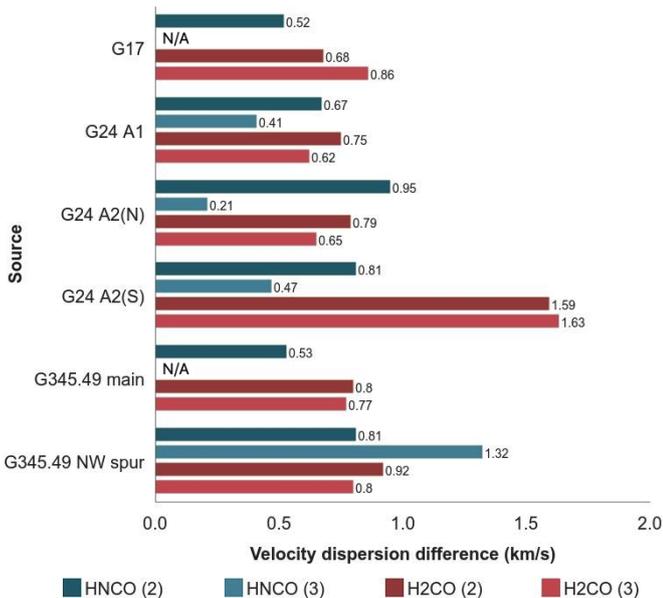
Fig. 12. Average velocity dispersion difference between NH$_2$CHO and transitions HNCO (2) and (3) and H$_2$CO (2) and (3). For the G24 sources HNCO (1) is used instead of HNCO (2).

consider the difference between H$_2$CO (2) and (3) as the error for these measurements.

3.4. Comparison of column densities and excitation temperatures

Using the XCLASS LTE spectral modeling software described in Sect. 2.3, we determine excitation temperature (T_{ex}), column densities (N_{col}), line width (FWHM), and velocity (v_{LSR}) for spectra extracted from single pixels (indicated in Fig. 1). Modeled N_{col} values were divided by the H$_2$ column densities listed in Table 2 to obtain abundances for comparison, and output v_{LSR} were subtracted from the v_{LSR} of the sources listed in Table 1 to obtain velocity offsets. The full modeling results are presented in Tables 8–10. The errors shown were determined using the *errorestim_ins* algorithm using the Markov chain Monte Carlo (MCMC) method built into the XCLASS software. A detailed description of this method is included in the XCLASS manual[4].

Figure 16 shows the modeled abundance values (X) for NH$_2$CHO, H$_2$CO, and HNCO plotted against each other for all subsources. The relationships between each of the species pairs

---

[4] Manual downloadable from: https://xclass.astro.uni-koeln.de/sites/xclass/files/pdfs/XCLASS-Interface_Manual.pdf
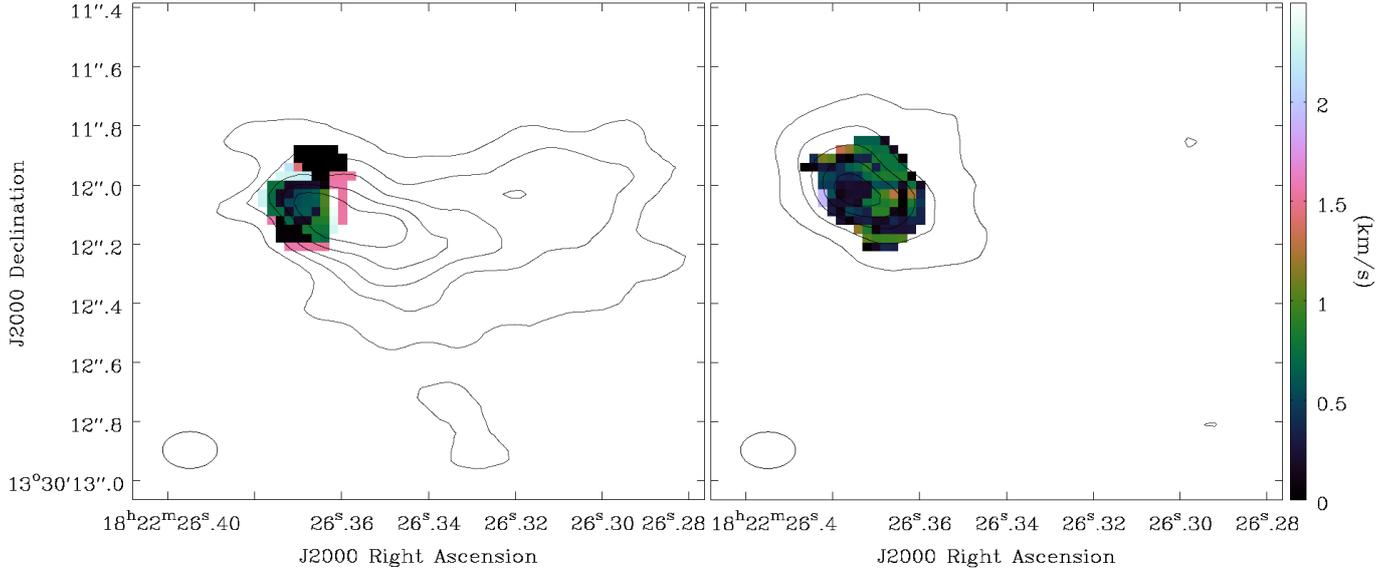
Fig. 13. Velocity dispersion difference (from second moment maps) at each pixel in G17 between (*left*) H_2CO (2) and NH_2CHO (1) and (*right*) HNCO (2) and NH_2CHO (1). The contours show the integrated intensity maps for H_2CO (2) and HNCO (2) as in Fig. 4. The velocity scale is the same for both panels.
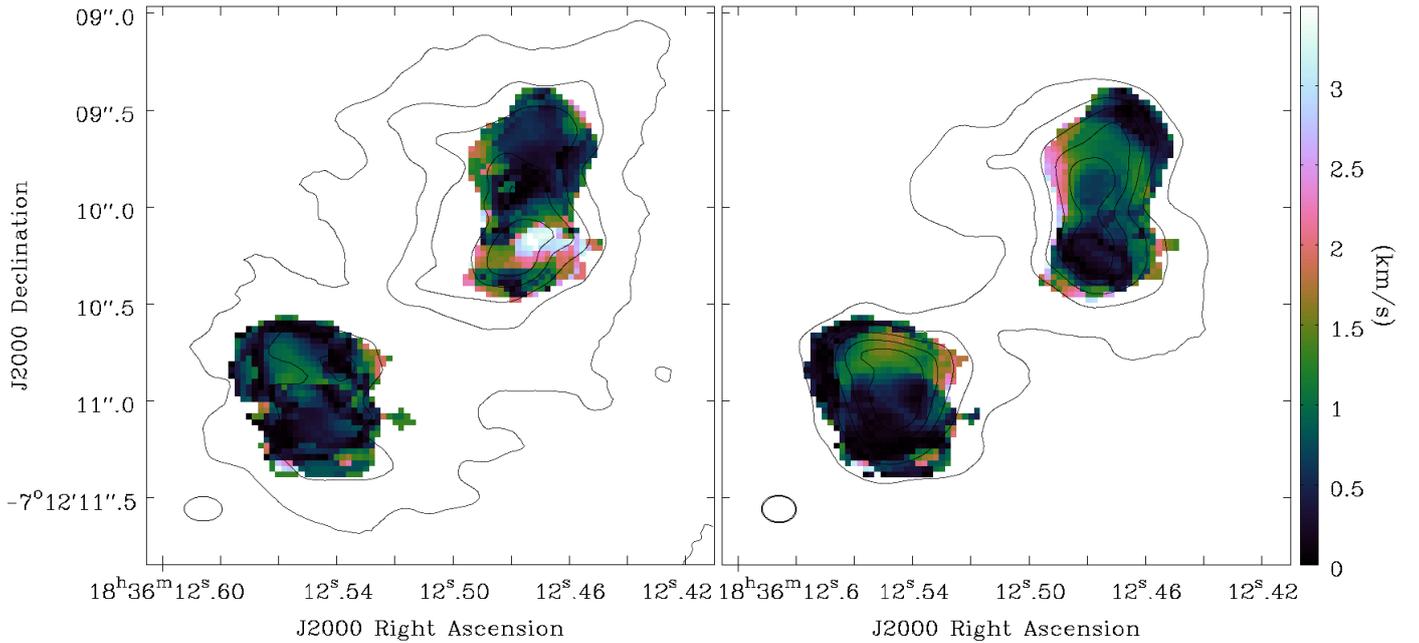
Fig. 14. Velocity dispersion difference (from second moment maps) at each pixel in G24 between (*left*) H_2CO (3) and NH_2CHO (2) and (*right*) HNCO (1) and NH_2CHO (2). The contours show the integrated intensity maps for H_2CO (3) and HNCO (1) as in Fig. 5. The velocity scale is the same for both panels.

all have good fits, all with an R^2 (a statistical measurement of linear correlation where 1 is best and values over 0.7 are considered well correlated.) greater than 0.93 with a slightly better correlation between H_2CO and NH_2CHO is best at 0.943. The fit for NH_2CHO vs. H_2CO is $[X(NH_2CHO) = 0.618\ X(H_2CO)^{1.103}]$ and the fit for NH_2CHO vs. HNCO is $[X(NH_2CHO) = 0.06\ X(HNCO)^{0.95}]$ $(R^2 = 0.93)$. The abundances of HNCO and H_2CO are also correlated with a fit of $[X(HNCO) = 4.796\ X(H_2CO)^{1.111}]$ $(R^2 = 0.936)$. The errors on the abundance are less than one order of magnitude, as seen in Fig. 16.

The T_{ex} and FWHM values do not show any correlation between any of the pairs of species, but both of these parameters

have a very narrow range of results for NH_2CHO. The T_{ex} range for NH_2CHO is 50–150 K, whereas for HNCO it is 75–200 K and for H_2CO it is 70–375 K. The largest errors in T_{ex} are for HNCO around G345 Main at 63 K, but the average error in T_{ex} is 12.7 K. The FWHM for NH_2CHO range from ~2.3–5.7 km s^{-1}, while for the other two the range is 2.8–6.5 km s^{-1}. The errors associated with the FWHM fits are very small with an average of 0.2 km s^{-1} with the largest error being 0.7 km s^{-1}.

Figure 17 shows the velocity offset values for NH_2CHO, HNCO, and H_2CO plotted against each other for all subsources. The scatter of velocity offset values for NH_2CHO is smaller with HNCO than with H_2CO (R^2 of 0.95 vs. 0.48). The slope
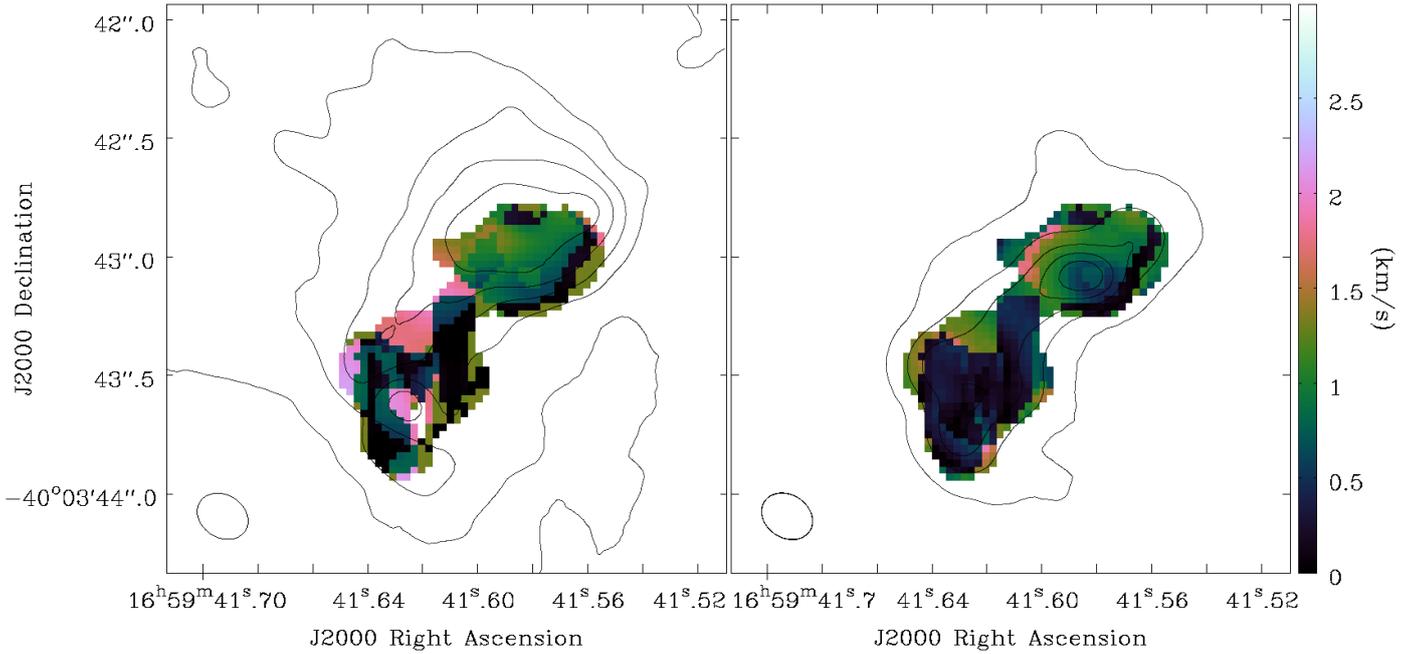
Fig. 15. Velocity dispersion difference (from second moment maps) at each pixel in G345 between (*left*) H$_2$CO (2) and NH$_2$CHO (1) and (*right*) HNCO (2) and NH$_2$CHO (1). The contours show the integrated intensity maps for H$_2$CO (2) and HNCO (2) as in Fig. 6. The velocity scale is the same for both panels.

of the NH$_2$CHO vs. HNCO velocity offset plot is nearly 1, but the intercept is not zero ($V_{\mathrm{NH2CHO}} = 1.31\ V_{\mathrm{HNCO}} - 0.68$) whereas the slope of NH$_2$CHO vs. H$_2$CO is closer to 0.7 but the intercept is nearer to zero ($V_{\mathrm{NH2CHO}} = 0.69\ V_{\mathrm{H2CO}} + 0.39$). The errors on the model fit of velocity offset are also small where the largest is 0.9 km s^{-1} but the average error for all sources and species is 0.3 km s^{-1}.

4. Discussion

4.1. Overall map trends

We see from the summary of map analysis results in Table 7 that the peak positions and dispersion maps favor HNCO slightly over H$_2$CO in similarity with NH$_2$CHO and the velocity dispersion maps for HNCO are almost always most similar to NH$_2$CHO. There are two sources which favor HNCO over H$_2$CO in all three moment map tests: G24 A1 and G345 Main. While the integrated emission peaks of HNCO are generally much closer to NH$_2$CHO (by 0.1–0.3″), differences of less than 0.2″ are smaller than the beam. We measure the 2D-Gaussian peaks of the lines with an error of 0.01″ so the similarity between HNCO and NH$_2$CHO peaks is significant. The gas velocity structure of NH$_2$CHO is closer to HNCO in half of the sources (G24 A1, G345 Main, and G345 NW spur), and closer to H$_2$CO in the other half (G17, G24 A2(N) and A2(S)), but the difference in gas velocities between H$_2$CO–NH$_2$CHO and HNCO–NH$_2$CHO is generally less than 0.2 km s^{-1} (as depicted in Fig. 8 and Table 5). With an error of the central velocity measurement of 0.4 km s^{-1} for NH$_2$CHO (1) (from Gaussian fits of this transition in each source), this difference is not significant for G17, and G345 Main and NW spur. For the subsources in G24 which use NH$_2$CHO (2), the error on the velocity measurement is 0.1 km s^{-1} (also from Gaussian fits), which makes the similarity between NH$_2$CHO and H$_2$CO in G24 A2(N) and between NH$_2$CHO and HNCO (3) in G24 A1 significant. The

velocity dispersion values for HNCO are closer to NH$_2$CHO for five sources but closer to H$_2$CO for one source and they typically span a larger range of velocities for H$_2$CO. From these overall results, it seems that HNCO has a slightly stronger relationship with NH$_2$CHO.

The opacity of the H$_2$CO transitions investigated here cannot be discounted. It is possible that the greater differences in spatial distribution, velocity, and dispersion between H$_2$CO and NH$_2$CHO compared to HNCO arise from optical depth issues. This is being investigated in a follow-up study involving isotopologues.

4.2. XCLASS analysis

The result of our XCLASS analysis shows no relationship between the widths of lines of different species or between the gas temperatures (T_{ex}) of any of the species. The velocity offset relationship is strongest between HNCO and NH$_2$CHO with a nearly linear fit and a small scatter.

There is a correlation between abundances for all three pairs of species but the best fit is between H$_2$CO and NH$_2$CHO. Most interesting is the relationship between the abundances of HNCO and NH$_2$CHO in this work is almost exactly the same as that reported in López-Sepulcre et al. (2015). In their paper, the best power-law fit was $X(\mathrm{NH_2CHO}) = 0.04\ X(\mathrm{HNCO})^{0.93}$ and the best fit in this work is $X(\mathrm{NH_2CHO}) = 0.06(\pm0.03)$ $X(\mathrm{HNCO})^{0.95(\pm0.05)}$. The correlation between abundances of all three pairs of species suggests that such a correlation is not a good indicator of a direct chemical relationship.

5. Conclusions

We present an observational study of two species potentially chemically related (HNCO and H$_2$CO) to NH$_2$CHO. Our study improves upon previous studies using single dish observations by including map analysis made possible using highly-sensitive
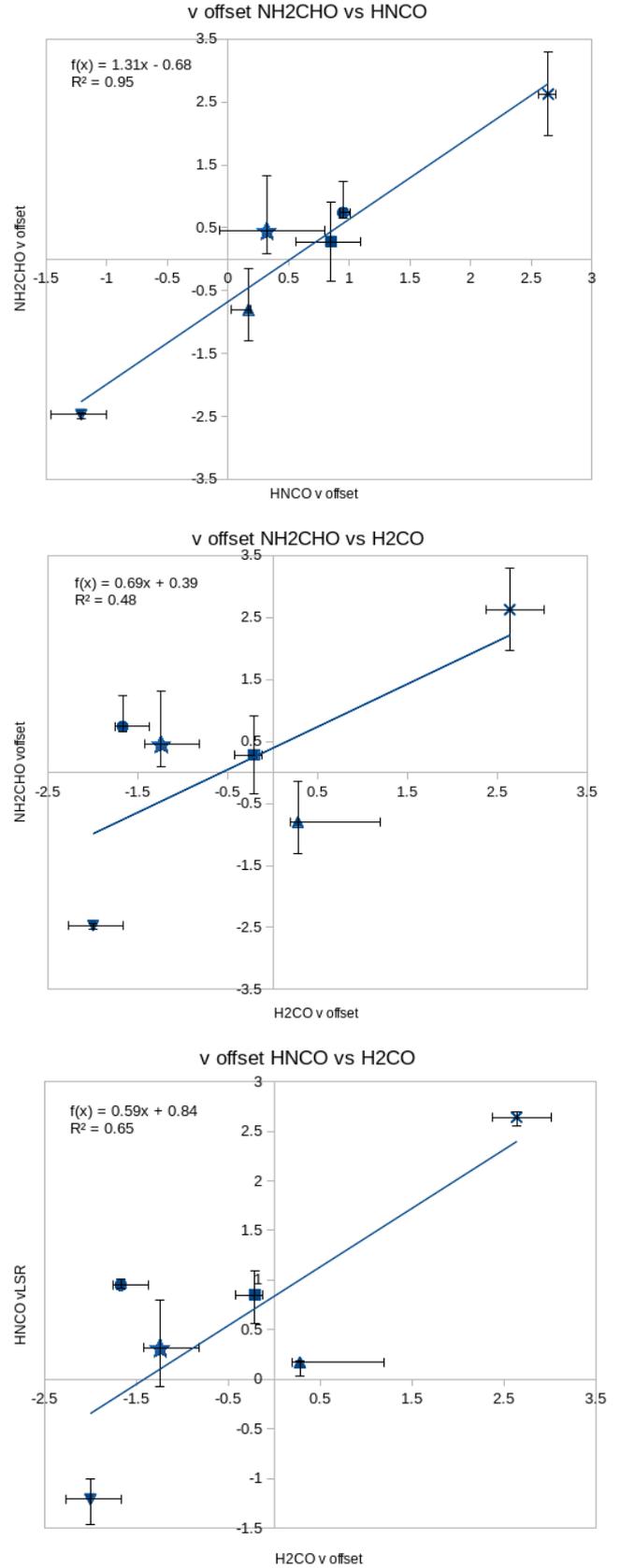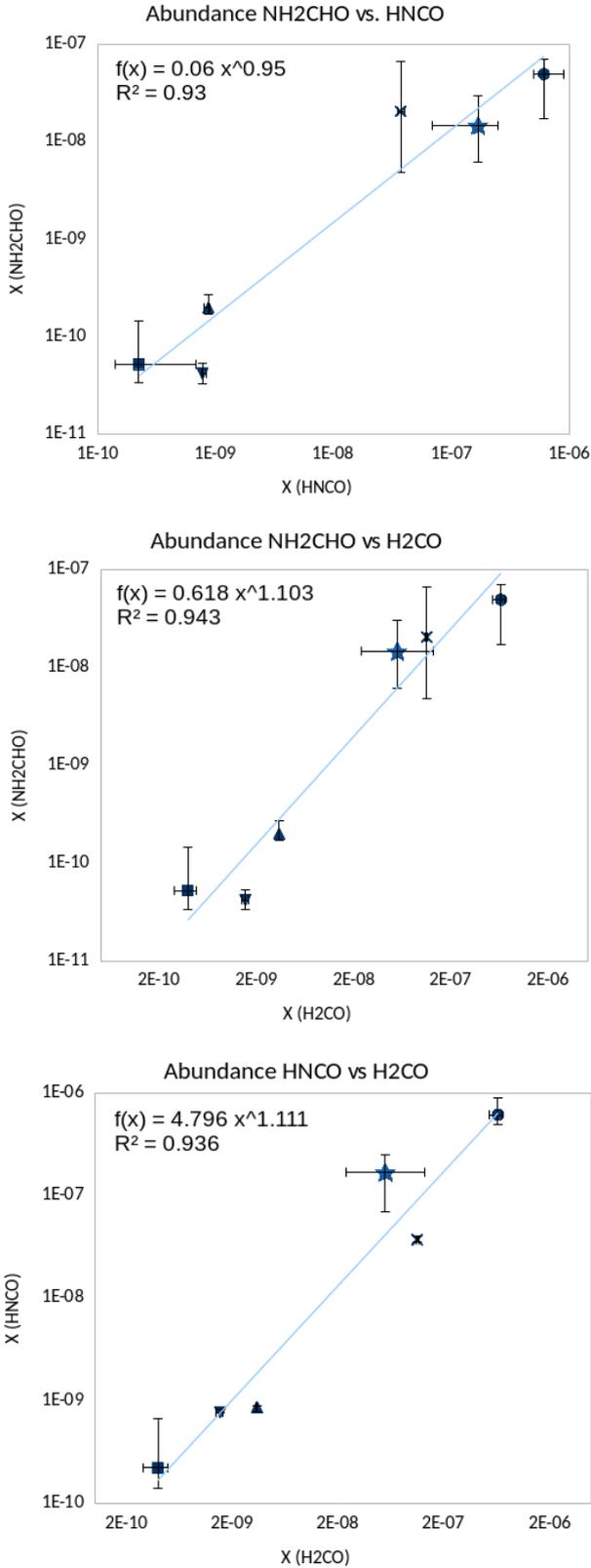
Fig. 16. XCLASS determined abundance comparison between NH$_2$CHO and HNCO (*top*), NH$_2$CHO and H$_2$CO (*middle*), and HNCO and H$_2$CO (*bottom*). The symbols correspond to different regions as follows: G17 is an upward triangle, G24 A1 is an "x", G24 A2(N) is a star, G24 A2(S) is a circle, G345 Main is a square, and G345 NW spur is a downward triangle.

Fig. 17. XCLASS determined velocity offset comparison between NH$_2$CHO and HNCO (*top*), NH$_2$CHO and H$_2$CO (*middle*), and HNCO and H$_2$CO (*bottom*). The symbols are as in Fig. 16.

Table 7. Summary of results from map analyses.

Source	HNCO Peak	HNCO Velocity	HNCO Dispersion	H$_2$CO Peak	H$_2$CO Velocity	H$_2$CO Dispersion
G17		=	✓	✓	=	
G24 A1	✓	✓	✓			
G24 A2(N)	✓		✓		✓	
G24 A2(S)	=	=	✓	=	=	
G345 Main	✓	=	✓		=	
G345 NW spur	✓	=	=		=	=

Notes. The check symbol (✓) indicates the species with the emission peak closest to the NH$_2$CHO peak, velocity-difference histogram center nearest to zero, or dispersion-difference histogram center nearest to zero. Equals signs (=) indicate that the parameters were equal for both HNCO and H$_2$CO within errors.

Table 8. XCLASS LTE spectral modeling results for formamide (NH$_2$CHO).

NH$_2$CHO Source	T_{ex}	−	+	N_{col}	Lower limit	Upper limit	Δv	−	+	v_{LSR}	−	+
G17	56.23	0.29	0.44	2.09×10^{15}	1.78×10^{15}	2.88×10^{15}	5.7	0.3	0.2	23.3	0.5	0.65
G24 A1	65	14	26	2.77×10^{16}	6.49×10^{15}	8.96×10^{16}	3.1	0.2	0.2	108.4	0.7	0.7
G24 A2(N)	79	13	15	1.45×10^{16}	6.06×10^{15}	2.97×10^{16}	3.3	0.1	0.1	110.5	0.4	0.9
G24 A2(S)	89	20	2	2.42×10^{15}	1.41×10^{15}	5.75×10^{15}	2.5	0.1	0.3	110.3	0.1	0.5
G345 Main	152	33	27	5.13×10^{15}	3.31×10^{15}	1.41×10^{16}	2.4	0.6	0.5	−17.8	0.6	0.6
G345 NW spur	93	4	10	9.68×10^{14}	7.69×10^{14}	1.22×10^{15}	3.3	0.2	0.2	−12.03	0.06	0.03

Notes. Columns show modeled excitation temperature (T_{ex}), column density (N_{col}), line width (Δv), and line velocity (v_{LSR}) for each of our key species. The columns indicated by a minus sign (−) indicate the error to the left of the result and those indicated by a plus sign (+) indicate the error to the right.

Table 9. XCLASS best fit results as in Table 8 but for HNCO.

HNCO Source	T_{ex}	−	+	N_{col}	Lower limit	Upper limit	Δv	−	+	v_{LSR}	−	+
G17	86	4	1	9.12×10^{15}	8.32×10^{15}	9.33×10^{15}	6.17	0.03	0.19	22.67	0.14	0.02
G24 A1	192.0	0	1	5.01×10^{16}	4.79×10^{16}	5.37×10^{16}	6.43	0.06	0.31	108.4	0.08	0.06
G24 A2(N)	177.0	18	27	1.66×10^{17}	6.77×10^{16}	2.46×10^{17}	3.28	0.05	0.13	110.7	0.4	0.5
G24 A2(S)	114.9	0.7	3.7	5.02×10^{17}	4.08×10^{17}	7.43×10^{17}	3.63	0.01	0.1	110.1	0.03	0.06
G345 Main	173.0	27	63	2.19×10^{16}	1.38×10^{16}	6.61×10^{16}	5.0	0.7	0.3	−18.4	0.3	0.2
G345 NW spur	198.7	0.4	0.5	1.78×10^{16}	8.00×10^{14}	2.17×10^{15}	4.3	0.2	0.1	−13.3	0.3	0.2

interferometric observations. The different moment maps that we employ indicate whether the gas containing NH$_2$CHO has the same properties as the gas containing its potential precursors. The spectral analysis performed in López-Sepulcre et al. (2015) and Bisschop et al. (2007) used significantly more transitions and the rotational diagram method in order to determine abundances. While we had fewer unblended transitions available to us, the XCLASS LTE spectral modeling method is more rigorous and does not require the assumption of optically thin transitions as that would be incorrect. A few interferometric studies involving NH$_2$CHO have been done (e.g., Codella et al. (2017) – L1157-B1, Coutens et al. (2016) – IRAS 16293-2422), but only involving one of its precursors, so we also improve upon that method by

investigating the three species together in several star forming regions.

In our spectral modeling, we confirm the single dish relationship between the abundances of HNCO and NH$_2$CHO demonstrated in Bisschop et al. (2007) and López-Sepulcre et al. (2015) using interferometric observations. Our map analyses favor HNCO as chemically related to NH$_2$CHO. The abundance correlation between H$_2$CO and NH$_2$CHO is slightly stronger than the correlation between HNCO and NH$_2$CHO but both are very well correlated. It is possible that both formation processes are important in creating this species, or that different environments favor one process over the other. Dedicated studies using more transitions and isotopologues in a more diverse

Table 10. XCLASS best fit results as in Table 8 but for H$_2$CO.

H$_2$CO											
Source	T_{ex}	−	+	N_{col}	Lower limit	Upper limit	Δv	−	+	v_{LSR}	−	+
G17	110	1	3	3.58×10^{16}	3.51×10^{16}	3.59×10^{16}	4.26	0.06	0.23	22.78	0.08	0.92
G24 A1	374	5	6	1.51×10^{17}	1.47×10^{17}	1.55×10^{17}	6.4	0.1	0.3	108.4	0.3	0.4
G24 A2(N)	76	4	9	5.49×10^{16}	2.34×10^{16}	1.29×10^{17}	5.1	0.1	0.2	112.2	0.2	0.4
G24 A2(S)	138	30	46	5.33×10^{17}	4.42×10^{17}	5.89×10^{17}	4.6	0.3	0.2	112.38	0.03	0.75
G345 Main	188	4	33	3.86×10^{16}	2.81×10^{16}	4.77×10^{16}	2.9	0.6	0.7	−17.29	0.21	0.09
G345 NW spur	70	2	4	3.52×10^{16}	3.19×10^{16}	3.76×10^{16}	4.00	0.01	0.31	−12.5	0.3	0.3

selection of sources (high- and low-mass protostars, young stellar objects with disks, outflow regions, etc.) would shed light on this relationship.

References

Allen, V., van der Tak, F. F. S., Sánchez-Monge, Á., Cesaroni, R., & Beltrán, M. T. 2017, A&A, 603, A133

Barone, V., Latouche, C., Skouteris, D., et al. 2015, MNRAS, 453, L31

Beltrán, M. T., Cesaroni, R., Moscadelli, L., & Codella, C. 2007, A&A, 471, L13

Bisschop, S. E., Jørgensen, J. K., van Dishoeck, E. F., & de Wachter, E. B. M. 2007, A&A, 465, 913

Cesaroni, R., Sánchez-Monge, Á., Beltrán, M. T., et al. 2017, A&A, 602, A59

Charnley, S. B. 1997, IAU Colloq. 161, 89

Codella, C., Ceccarelli, C., Caselli, P., et al. 2017, A&A, 605, L3

Coutens, A., Jørgensen, J. K., van der Wiel, M. H. D., et al. 2016, A&A, 590, L6

Darla, N., & Sitha, S. 2019, J. Phys. Chem. A, 123, 8921

Endres, C. P., Schlemmer, S., Schilke, P., Stutzki, J., & Müller, H. S. 2016, J. Mol. Spectr., 327, 95

Fedoseev, G., Chuang, K.-J., van Dishoeck, E. F., Ioppolo, S., & Linnartz, H. 2016, MNRAS, 460, 4297

Guzmán, A. E., Garay, G., Rodríguez, L. F., et al. 2016, ApJ, 826, 208

Jones, B. M., Bennett, C. J., & Kaiser, R. I. 2011, ApJ, 734, 78

Kahane, C., Ceccarelli, C., Faure, A., & Caux, E. 2013, ApJ, 763, L38

Kaňuchová, Z., Boduch, P., Domaracka, A., et al. 2017, A&A, 604, A68

López-Sepulcre, A., Jaber, A. A., Mendoza, E., et al. 2015, MNRAS, 449, 2438

López-Sepulcre, A., Balucani, N., Ceccarelli, C., et al. 2019, ACS Earth Space Chem., 3, 2122

Lumsden, S. L., Hoare, M. G., Urquhart, J. S., et al. 2013, ApJS, 208, 11

Maud, L. T., Cesaroni, R., Kumar, M. S. N., et al. 2018, A&A, 620, A31

Mendoza, E., Lefloch, B., López-Sepulcre, A., et al. 2014, MNRAS, 445, 151

Möller, T., Endres, C., & Schilke, P. 2017, A&A, 598, A7

Moscadelli, L., Rivilla, V. M., Cesaroni, R., et al. 2018, A&A, 616, A66

Noble, J. A., Theule, P., Congiu, E., et al. 2015, A&A, 576, A91

Ossenkopf, V., & Henning, T. 1994, A&A, 291, 943

Quénard, D., Jiménez-Serra, I., Viti, S., Holdship, J., & Coutens, A. 2018, MNRAS, 474, 2796

Raunier, S., Chiavassa, T., Duvernay, F., et al. 2004, A&A, 416, 165

Reid, M. J., Menten, K. M., Brunthaler, A., et al. 2019, ApJ, 885, 131

Saladino, R., Crestini, C., Pino, S., Costanzo, G., & Di Mauro, E. 2012, Phys. Life Rev., 9, 84

Sánchez-Monge, Á., Beltrán, M. T., Cesaroni, R., et al. 2014, A&A, 569, A11

Sánchez-Monge, Á., Schilke, P., Ginsburg, A., Cesaroni, R., & Schmiedeke, A. 2018, A&A, 609, A101

Skouteris, D., Vazart, F., Ceccarelli, C., et al. 2017, MNRAS, 468, L1

van der Tak, F. F. S., Black, J. H., Schöier, F. L., Jansen, D. J., & van Dishoeck, E. F. 2007, A&A, 468, 627

Vichietti, R. M., Spada, R. F. K., da Silva, A. B. F., Machado, F. B. C., & Haiduke, R. L. A. 2019, ApJS, 245, 11

Appendix A: Formamide and ethanol in G345 NWspur
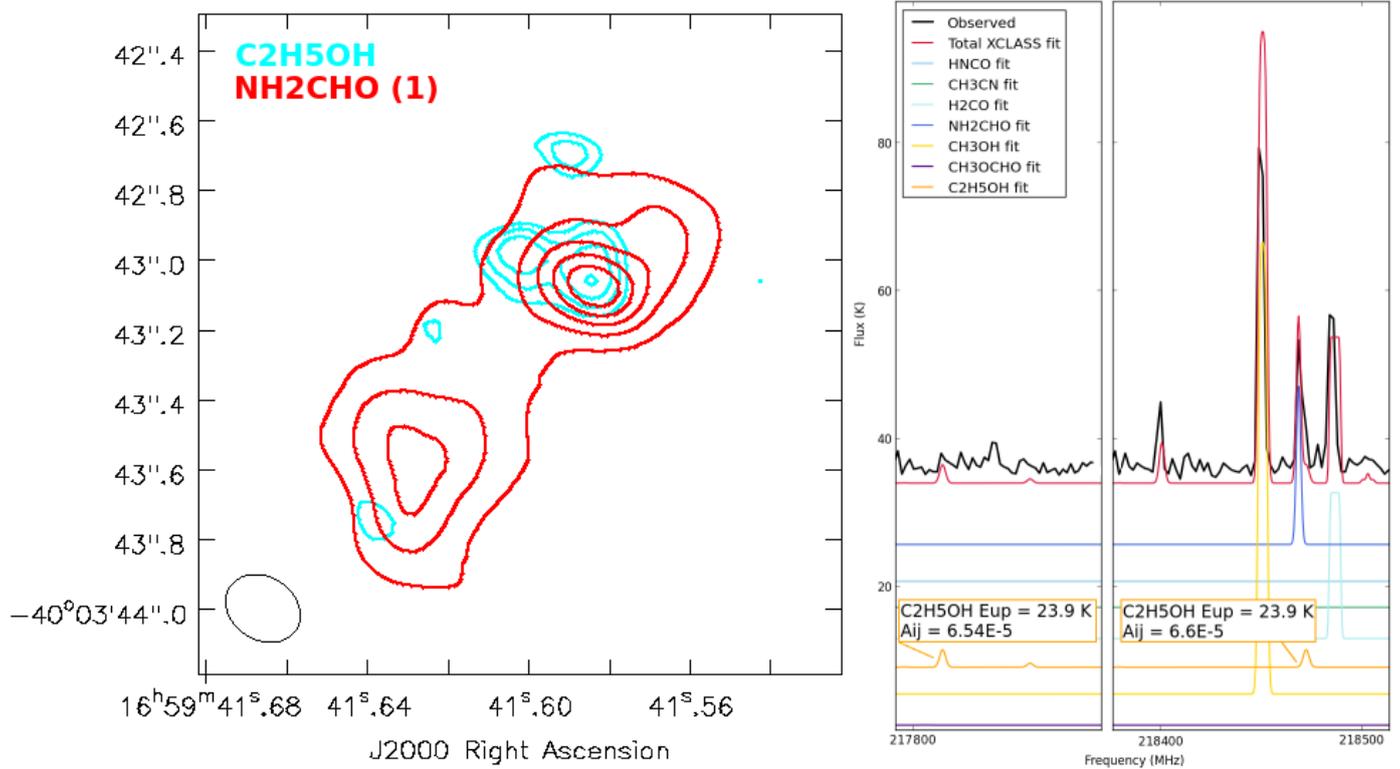
Fig. A.1. *Right*: spectrum of G345 NW spur showing a C_2H_5OH transition ($5_{3,3}$–$4_{2,2}$) at 217 803 MHz with the same E_{up} and nearly equal A_{ij} as the C_2H_5OH transition ($5_{3,2}$–$4_{2,3}$) that is blended with the NH_2CHO (1) transition (at 218 461 MHz). *Left*: contours of the integrated intensity map of this C_2H_5OH line is overlaid on the map of the NH_2CHO (1) transition to show that the strength and spatial extent is different.

## Appendix B: XCLASS fits
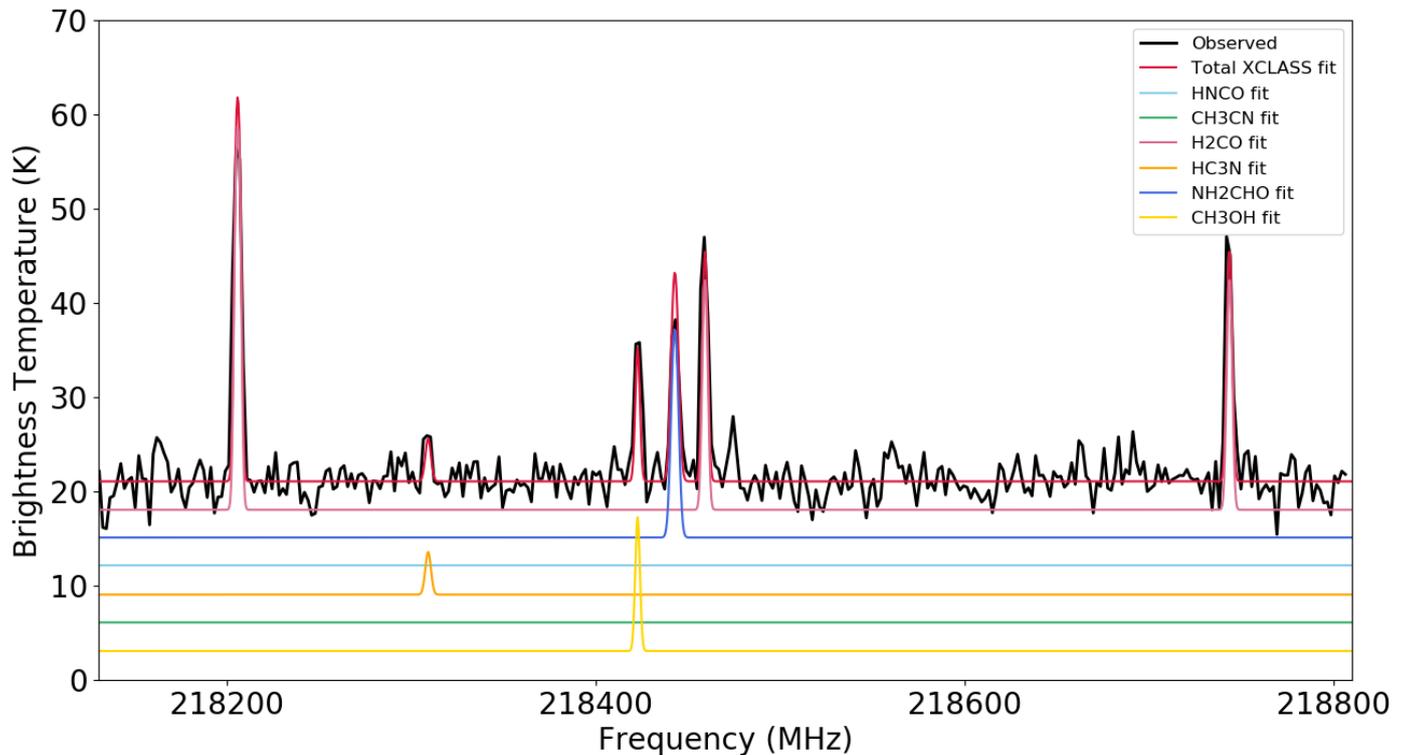
Fig. B.1. Spectral window from 218.1-218.8 GHz for G17 containing NH_2CHO (1) and H_2CO (1), (2), and (3).
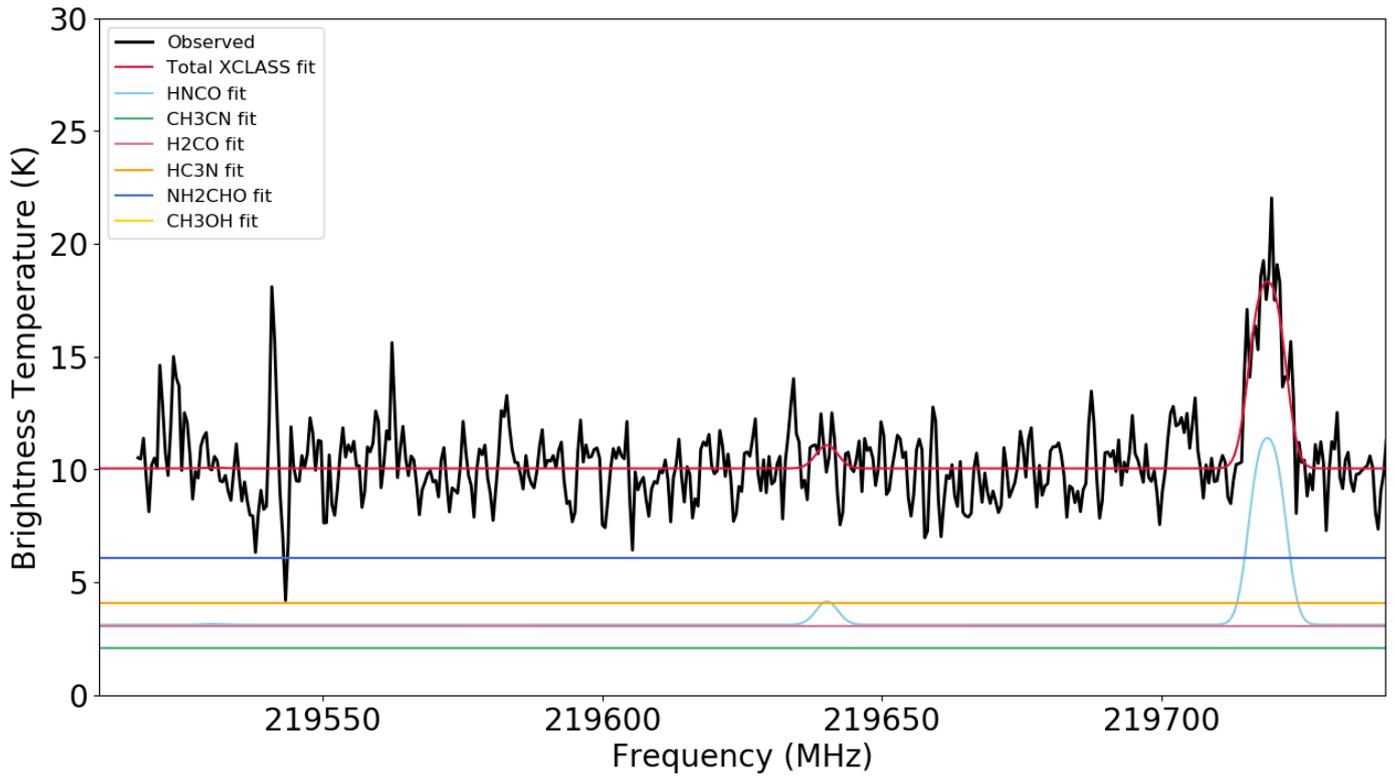
**Fig. B.2.** Spectral window from 219.5-219.8 GHz for G17 containing HNCO (3).
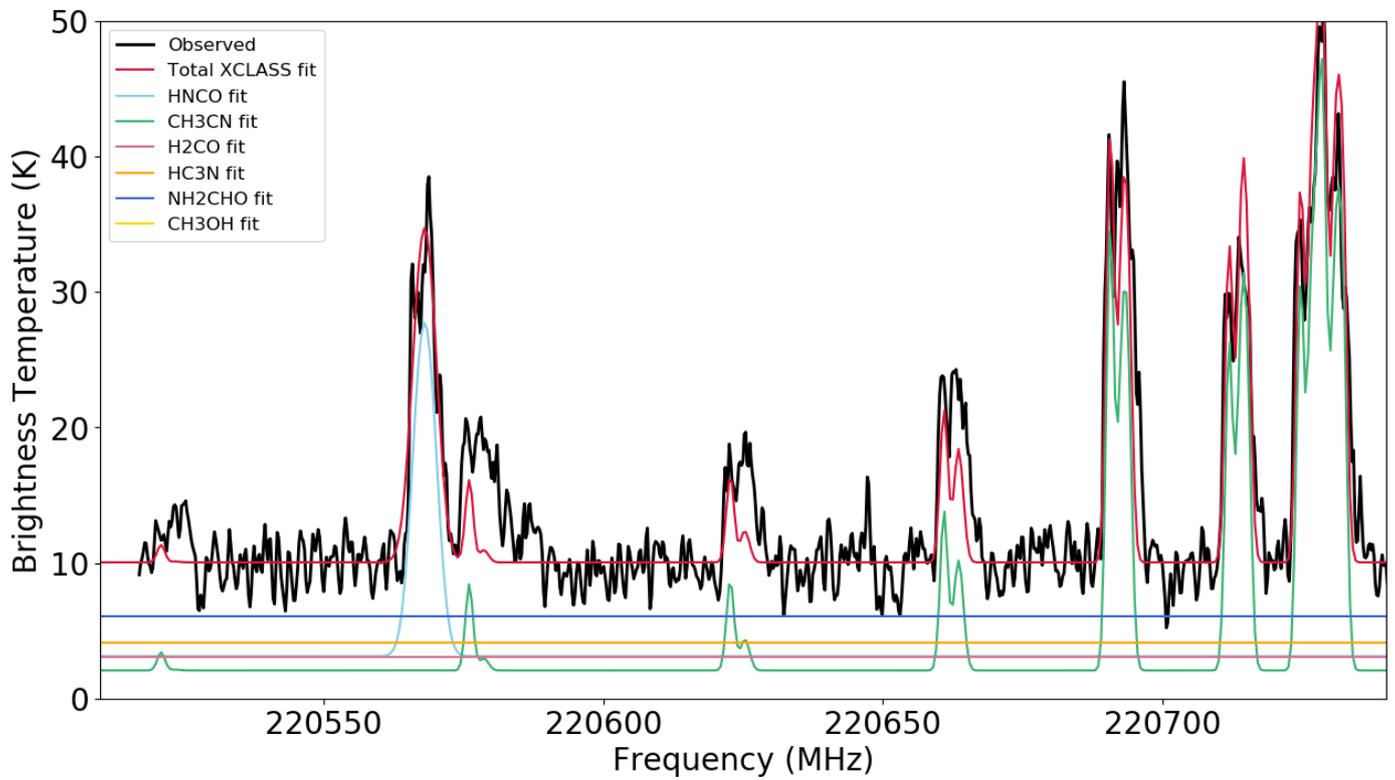
Fig. B.3. Spectral window from 220.5-220.75 GHz for G17 containing HNCO (2). We modeled two components for the CH₃CN emission (green) toward this source.
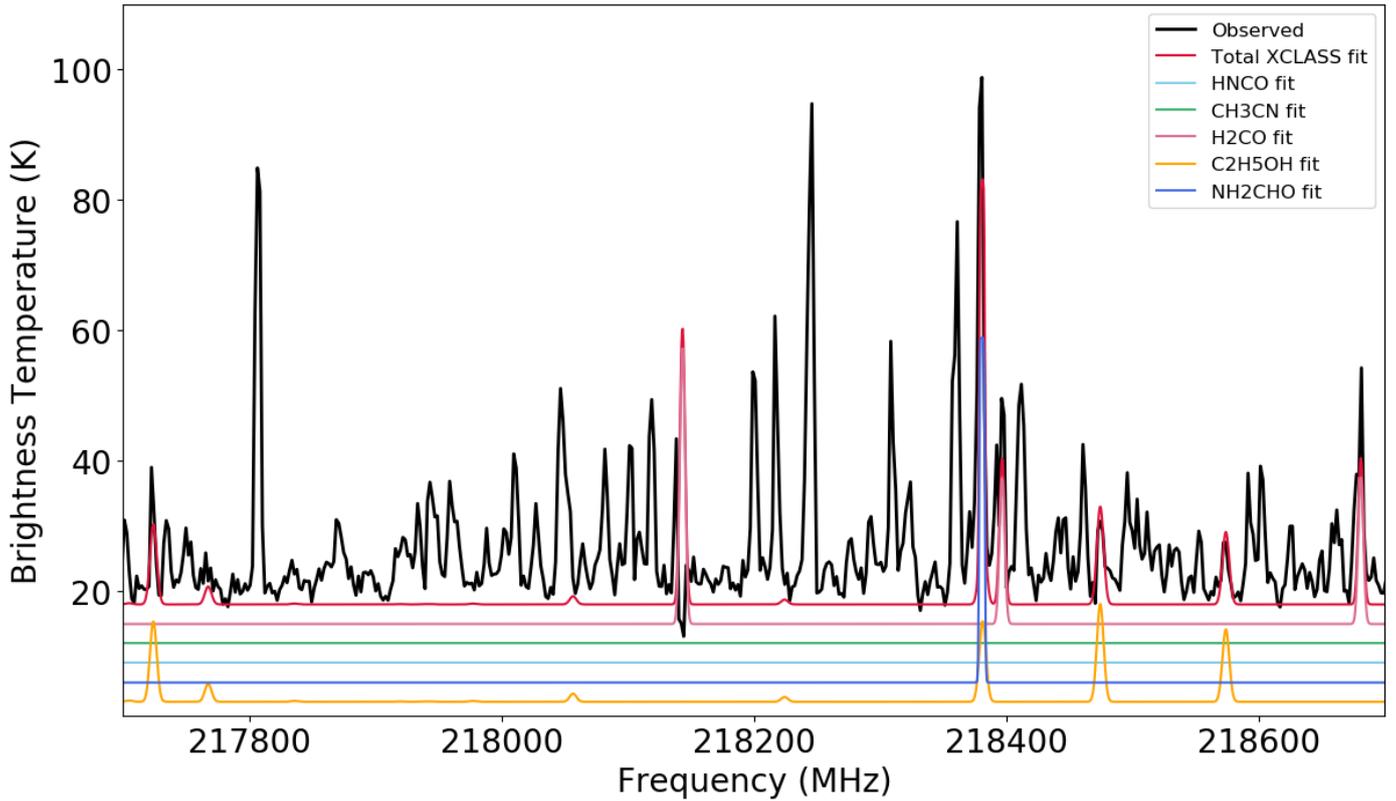
Fig. B.4. Spectral window from 217.7-218.7 GHz for G24 A1 containing NH_2CHO (1) and H_2CO (1), (2), and (3). NH_2CHO (1) is blended with a transition of C_2H_5OH.
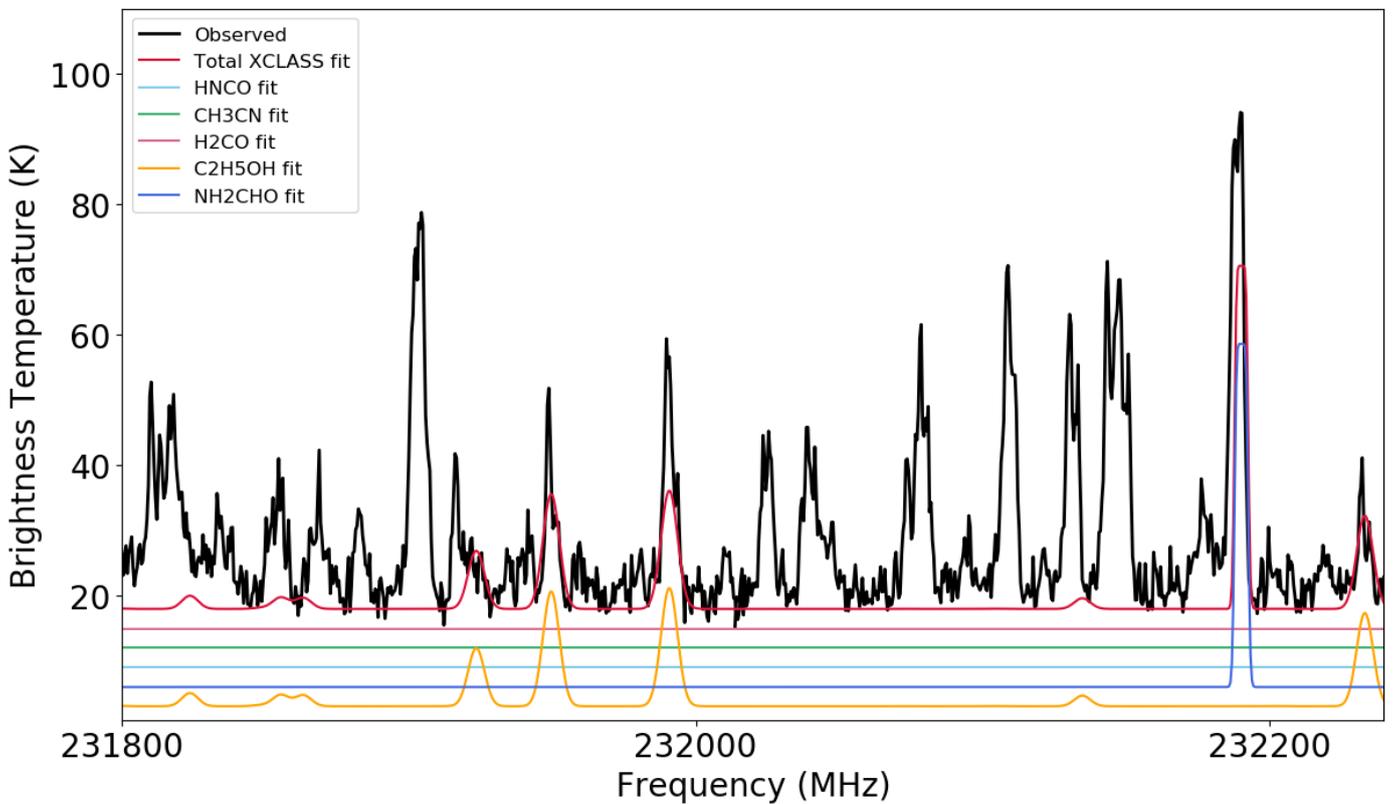
Fig. B.5. Spectral window from 231.8-232.3 GHz for G24 A1 containing NH_2CHO (2).
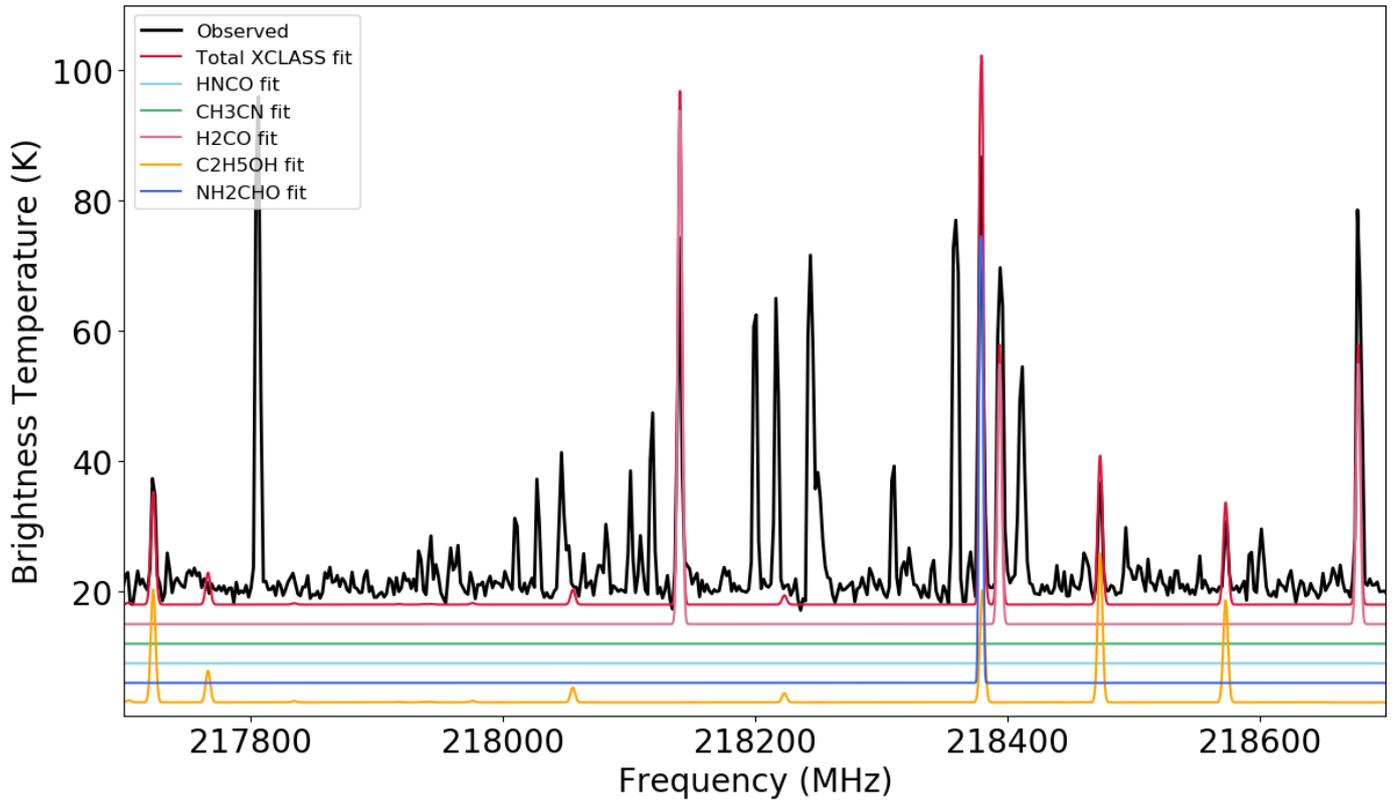
Fig. B.6. Spectral window from 217.7-218.7 GHz for G24 A2(N) containing NH_2CHO (1) and H_2CO (1), (2), and (3). NH_2CHO (1) is blended with a transition of C_2H_5OH.
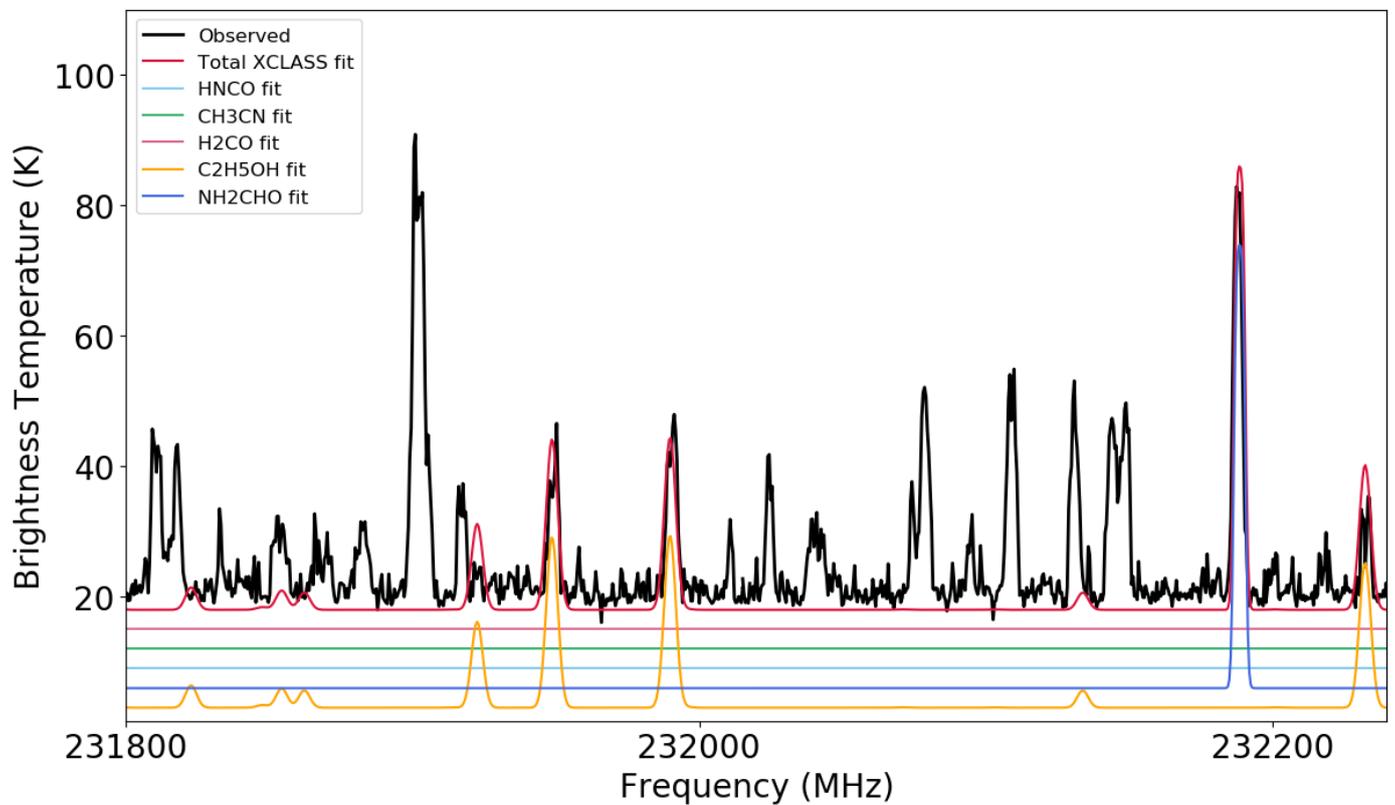
Fig. B.7. Spectral window from 231.8–232.3 GHz for G24 A2(N) containing NH_2CHO (2).
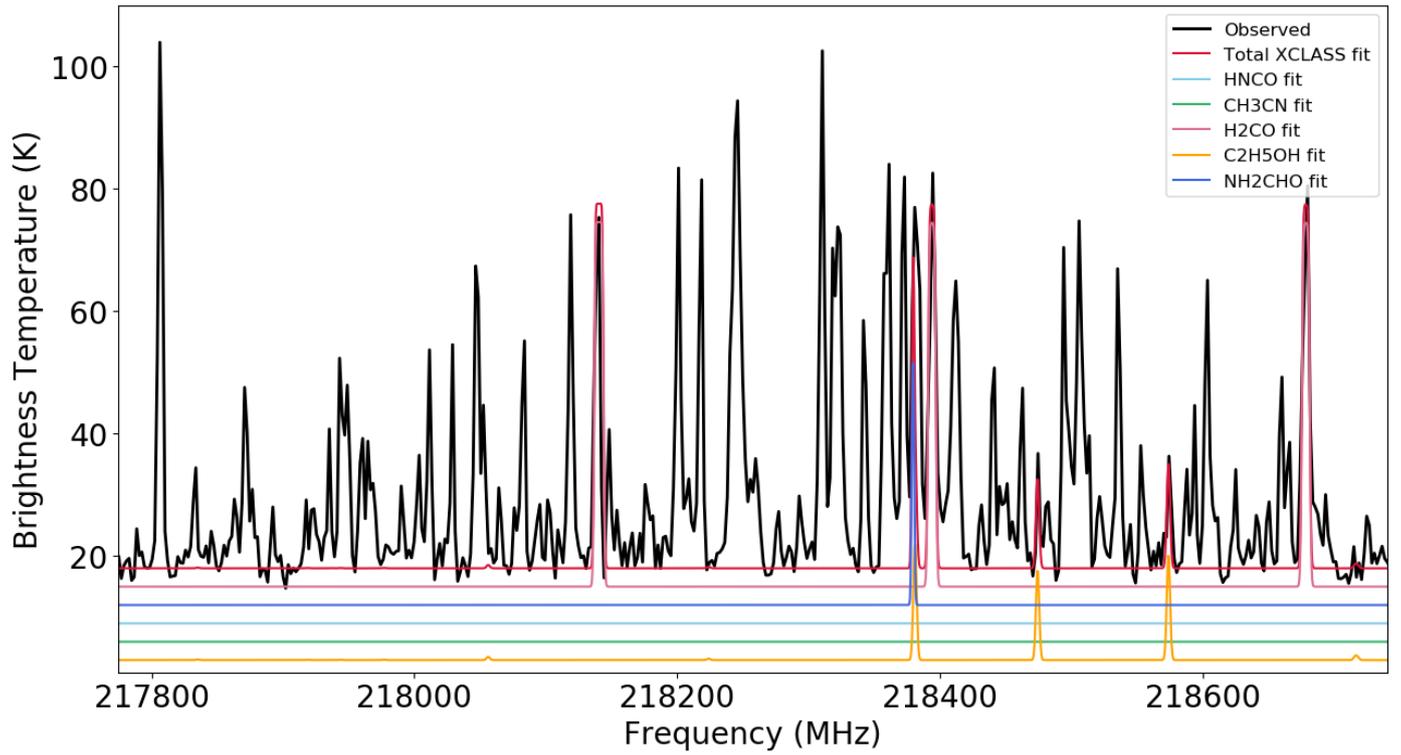
Fig. B.8. Spectral window from 217.7–218.7 GHz for G24 A2(S) containing NH_2CHO (1) and H_2CO (1), (2), and (3). NH_2CHO (1) is blended with a transition of C_2H_5OH.
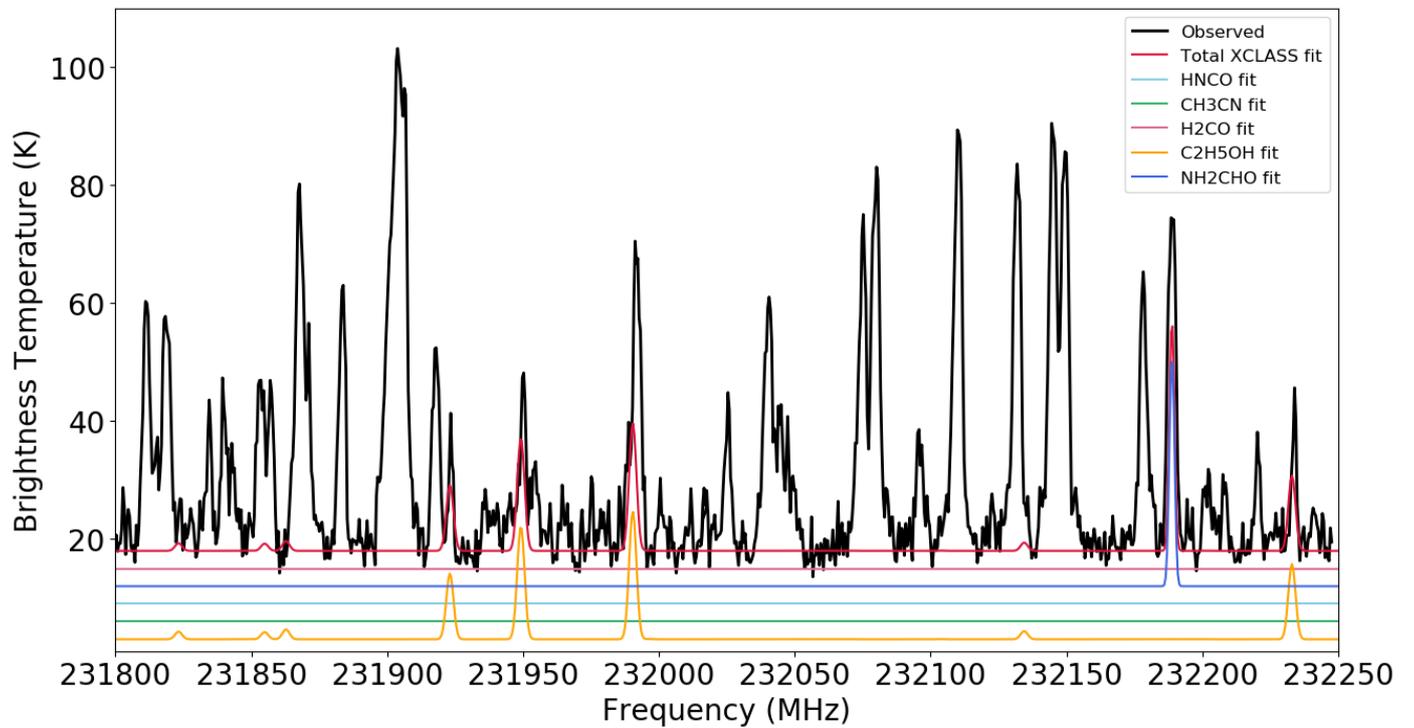
Fig. B.9. Spectral window from 231.8–232.3 GHz for G24 A2(S) containing NH_2CHO (2).
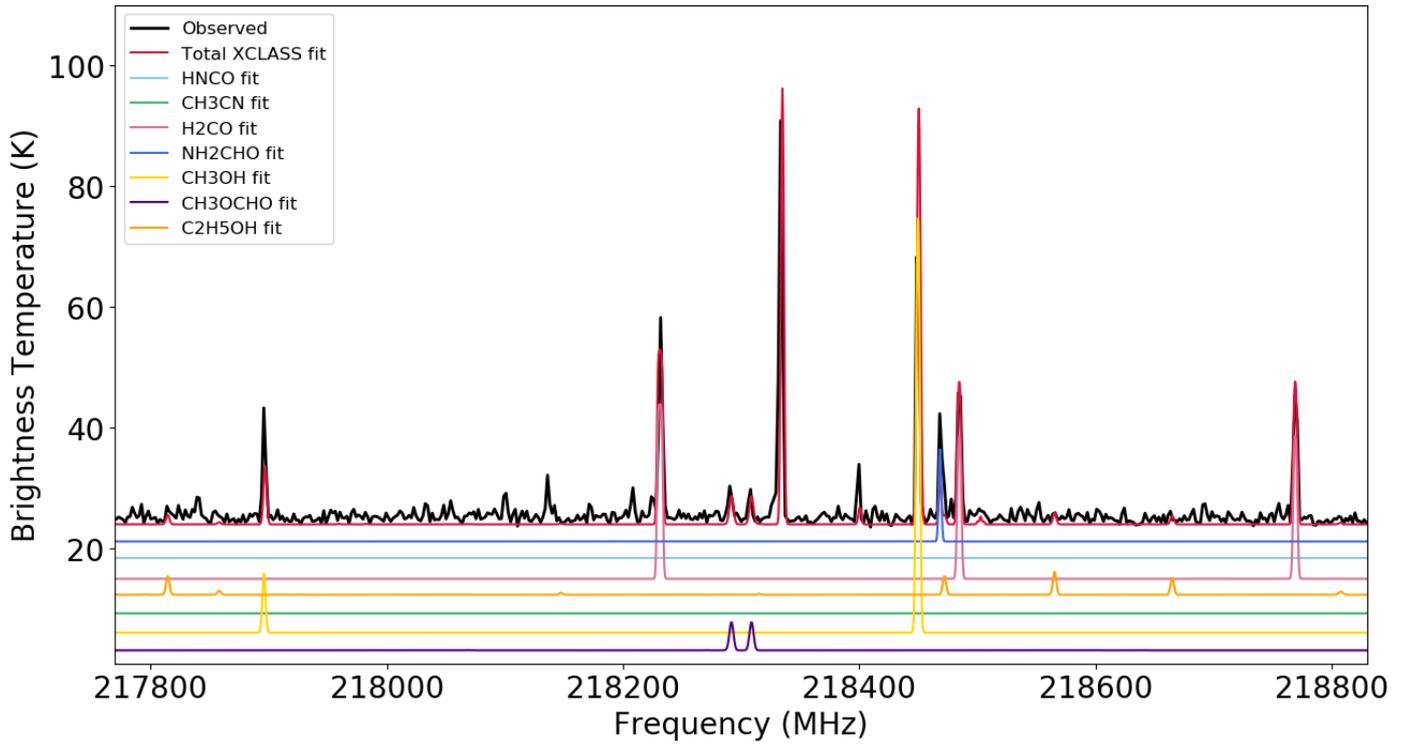
Fig. B.10. Spectral window from 217.8–218.8 GHz for G345 NW containing NH$_2$CHO (1) and H$_2$CO (1), (2), and (3).
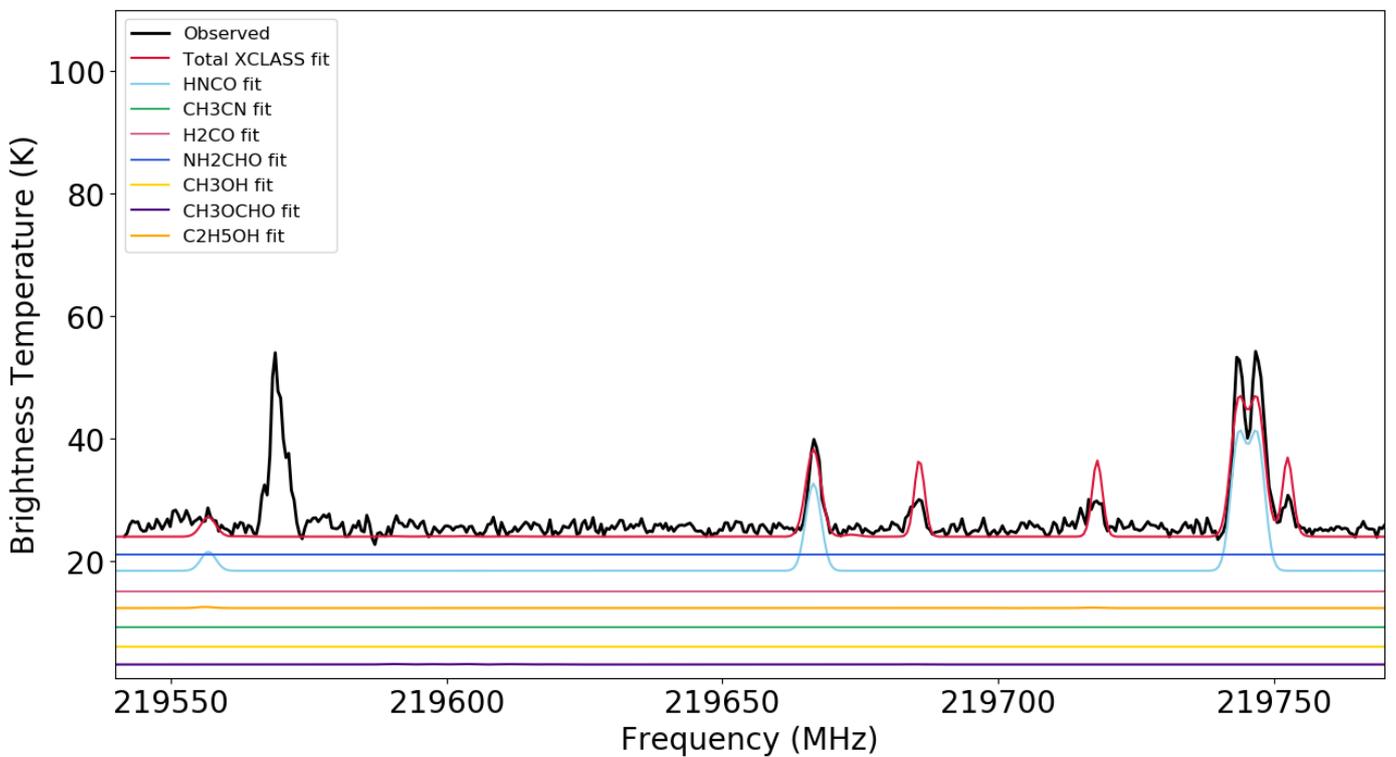
Fig. B.11. Spectral window from 219.5–219.8 GHz for G345 NW containing HNCO (3). The additional transitions shown in the total XCLASS fit are HC$_3$N (219 675 MHz), C$_2$H$_5$CN (219 699 MHz), and CH$_3$CHO (219 756 MHz).
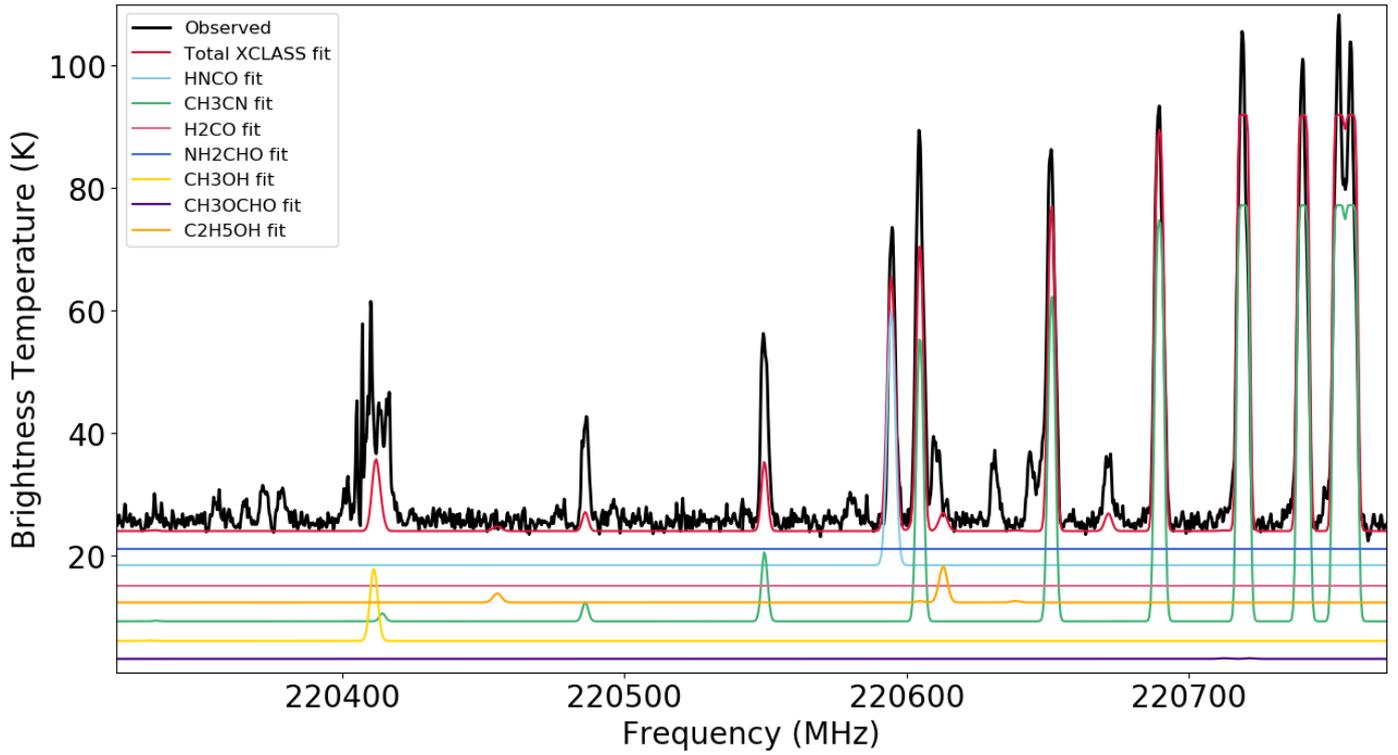
Fig. B.12. Spectral window from 220.3–220.8 GHz for G345 NW containing HNCO (2).
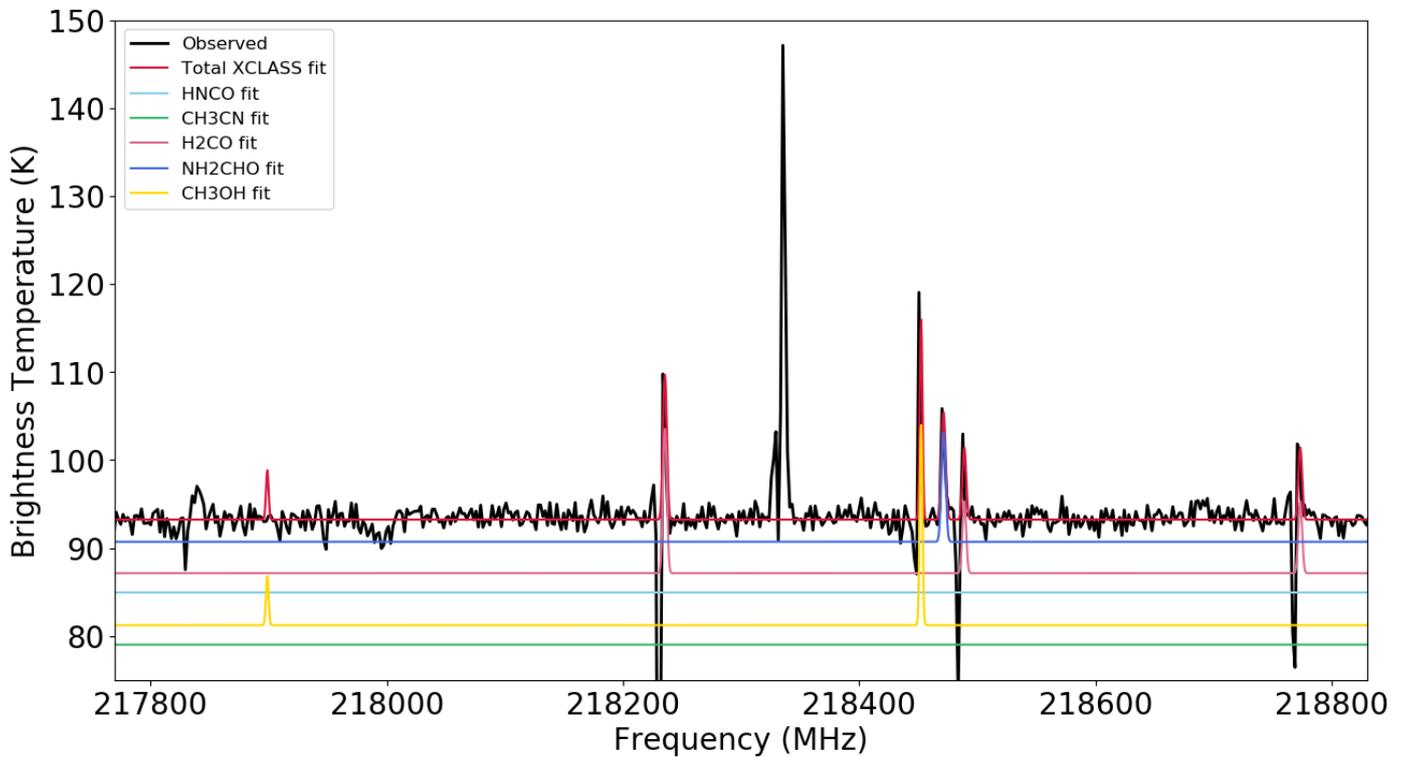
Fig. B.13. Spectral window from 217.8–218.8 GHz for G345 Main containing NH_2CHO (1) and H_2CO (1), (2), and (3).
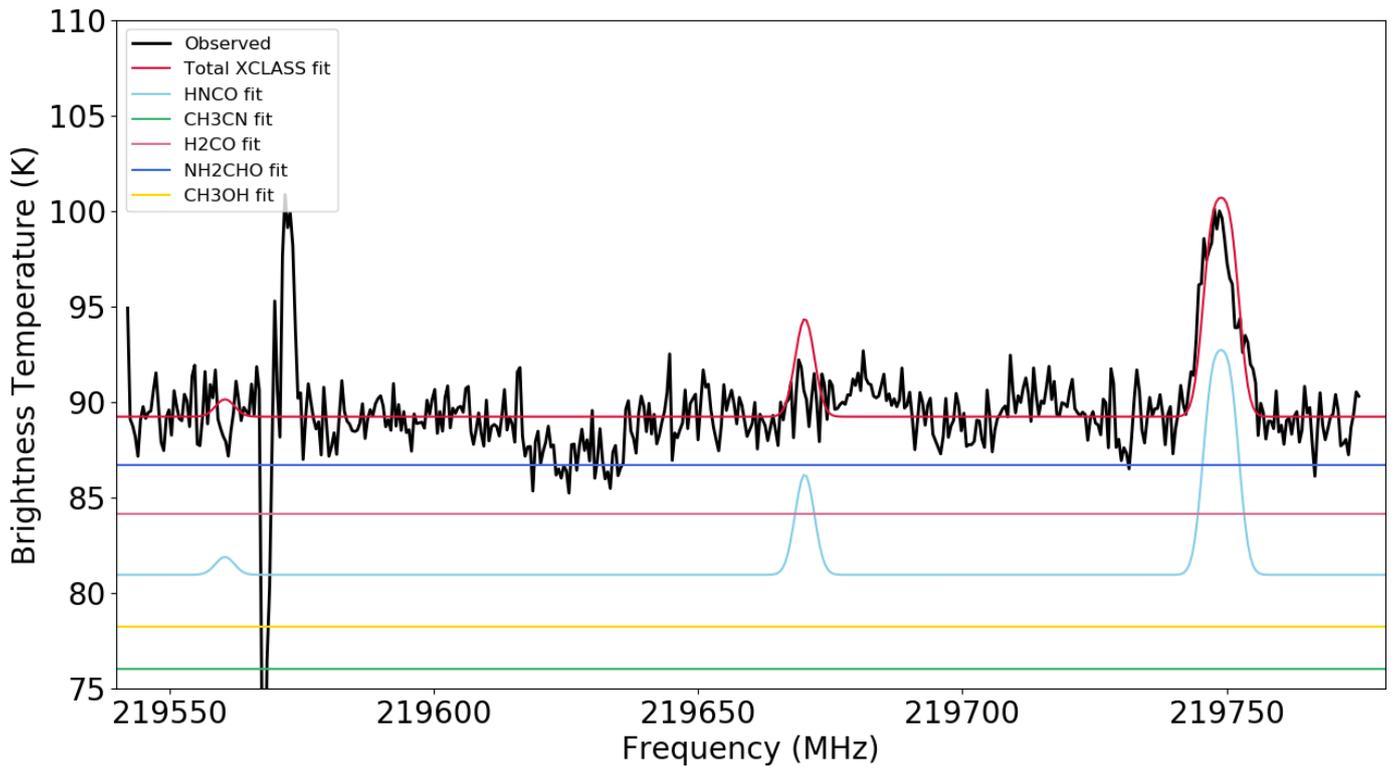
Fig. B.14. Spectral window from 219.5–219.8 GHz for G345 Main containing HNCO (3).
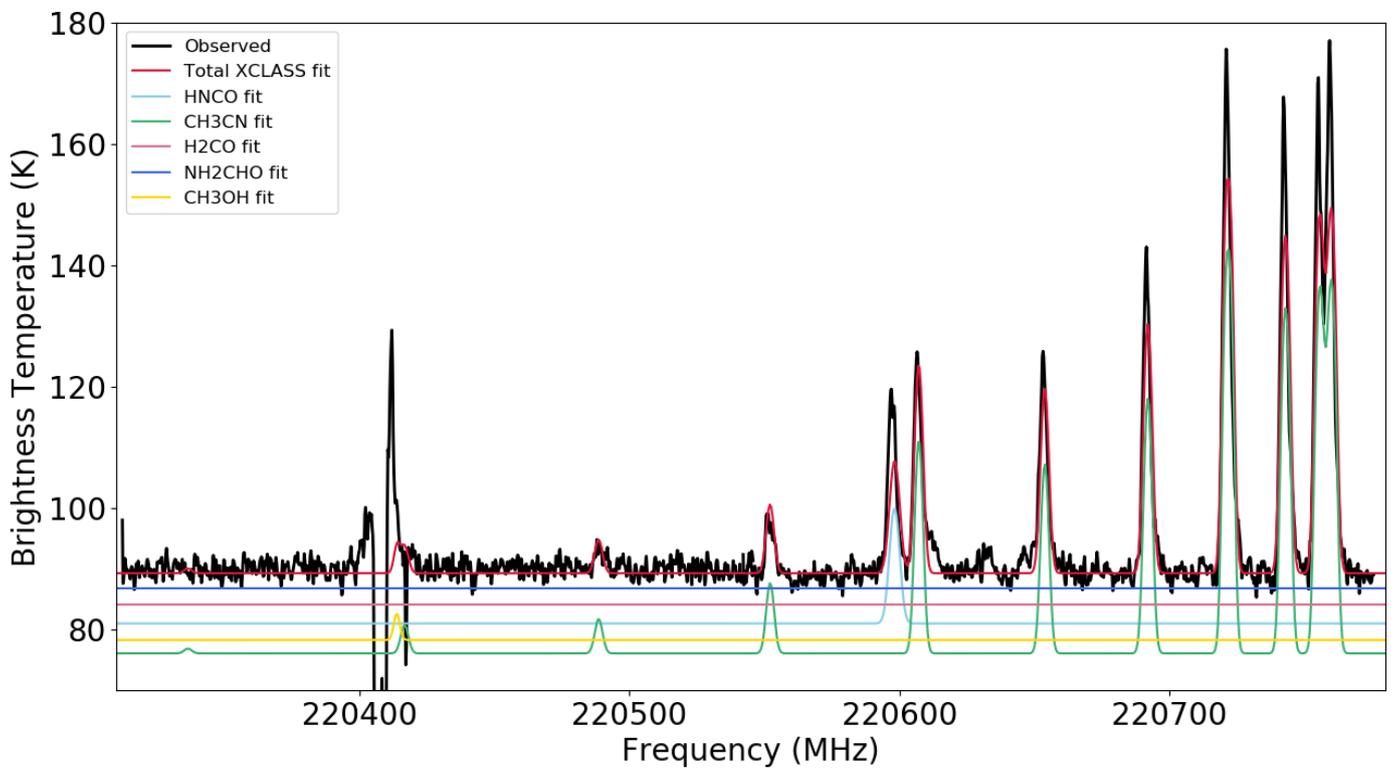
Fig. B.15. Spectral window from 220.3–220.8 GHz for G345 Main containing HNCO (2).

Appendix C: Histograms
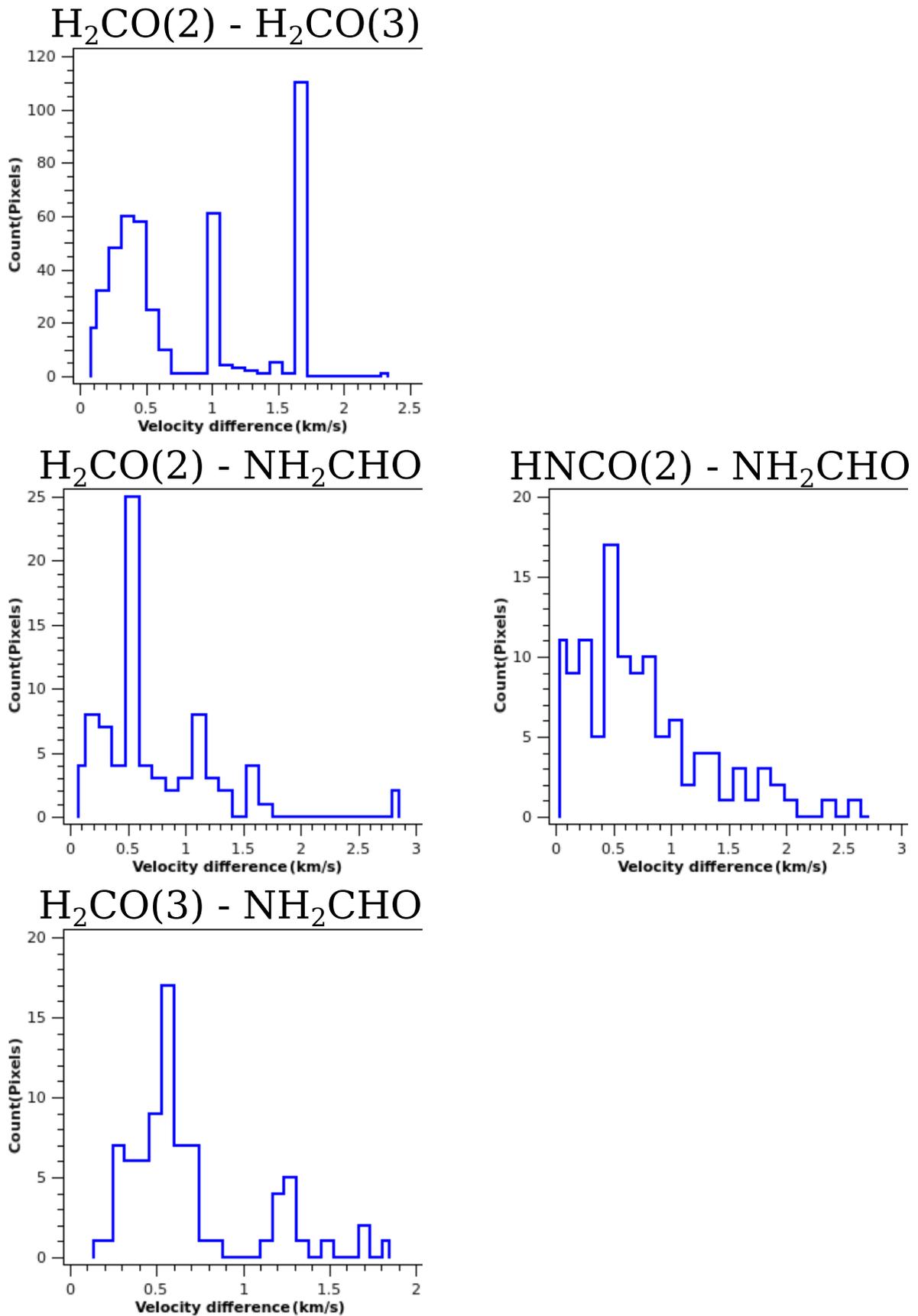

Fig. C.1. G17 first moment difference histogram.

H$_2$CO(2) - H$_2$CO(3)

HNCO(3) - HNCO(1)

H$_2$CO(2) - NH$_2$CHO

HNCO(1) - NH$_2$CHO

H$_2$CO(3) - NH$_2$CHO

HNCO(3) - NH$_2$CHO
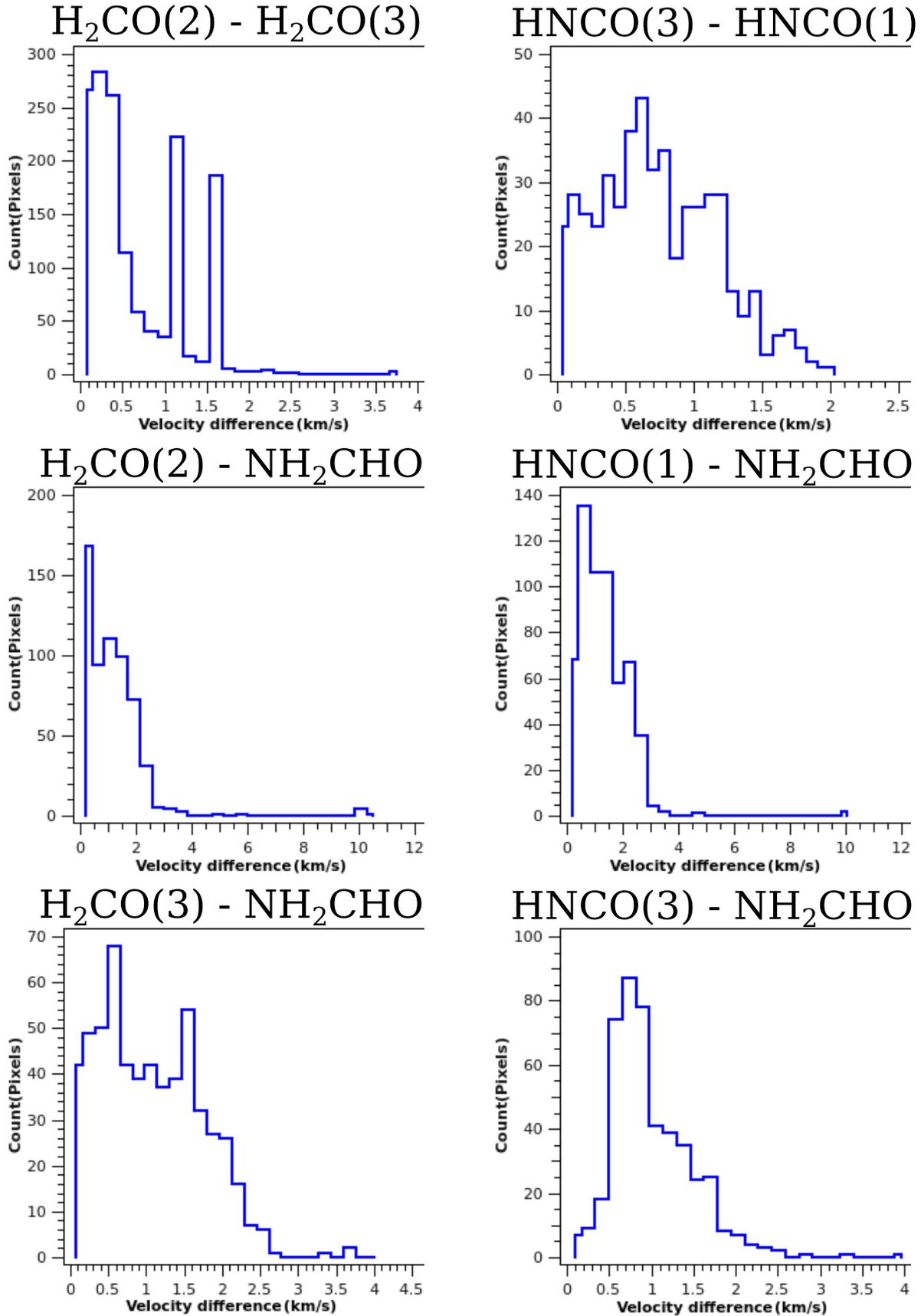
Fig. C.2. G24A1 first moment difference histogram.

H$_2$CO(2) - H$_2$CO(3)

HNCO(3) - HNCO(1)

H$_2$CO(2) - NH$_2$CHO

HNCO(1) - NH$_2$CHO

H$_2$CO(3) - NH$_2$CHO

HNCO(3) - NH$_2$CHO
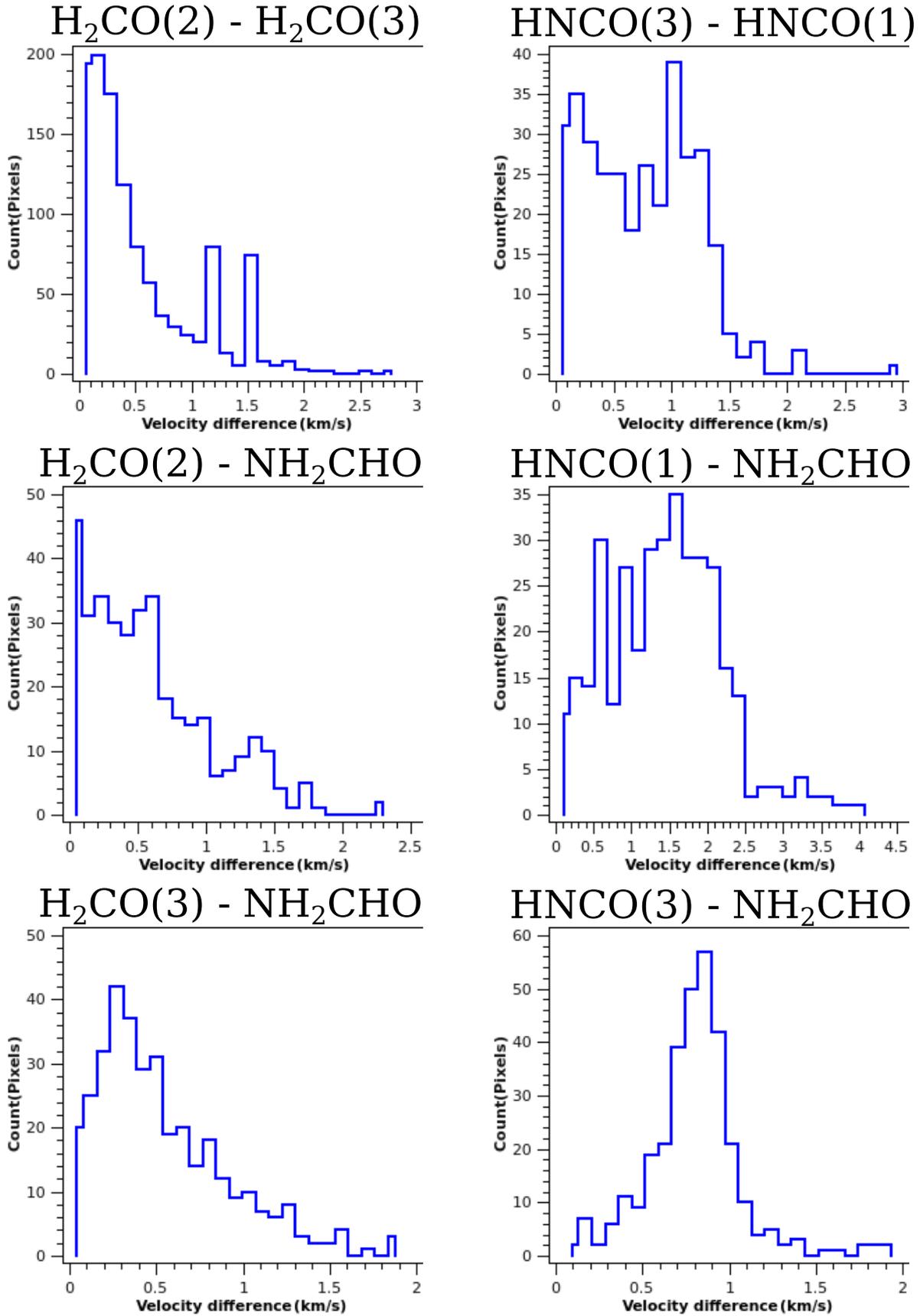
Fig. C.3. G24A2(N) first moment difference histogram.
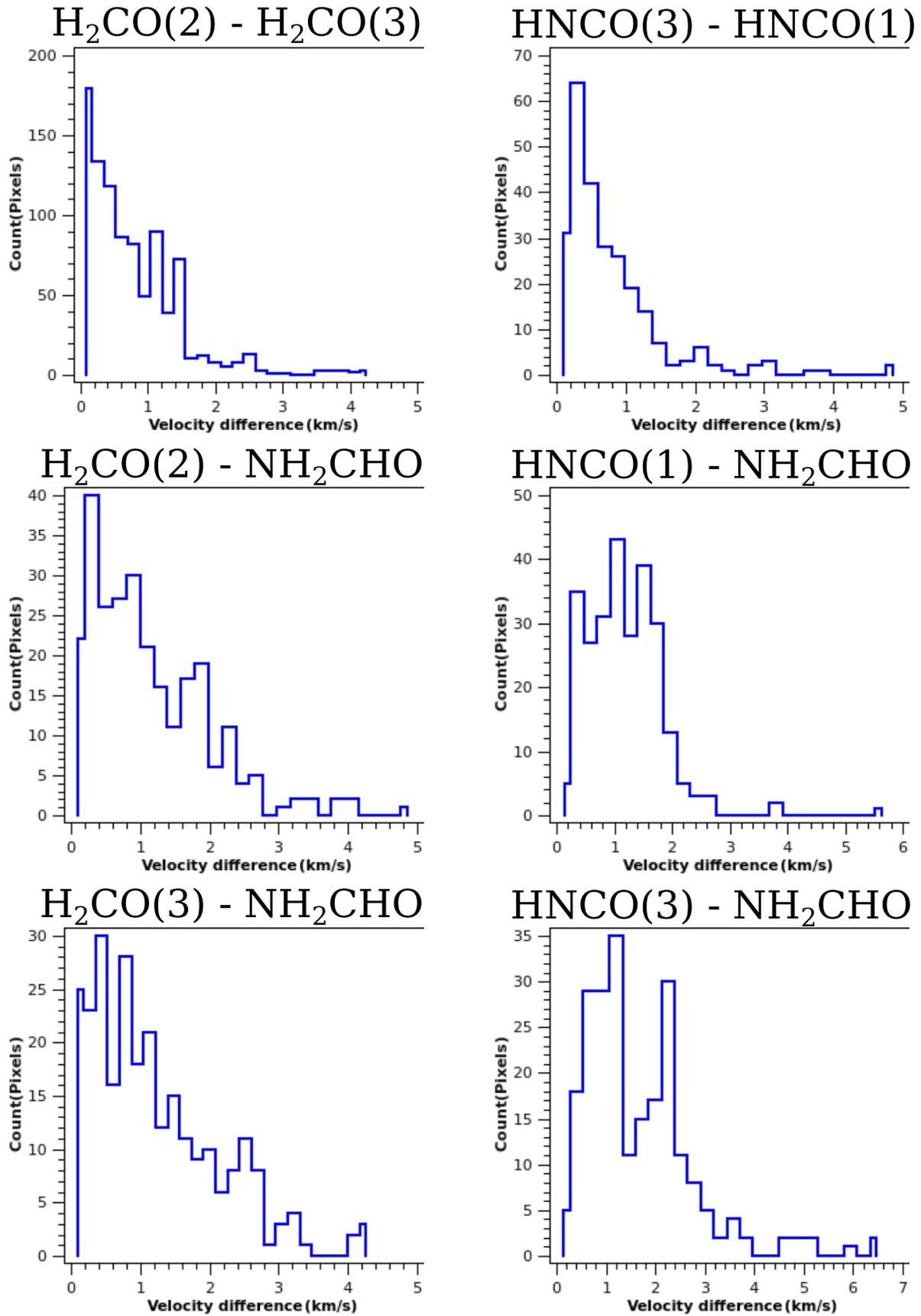
Fig. C.4. G24A2(S) first moment difference histogram.

H$_2$CO(2) - H$_2$CO(3)

H$_2$CO(2) - NH$_2$CHO

HNCO(2) - NH$_2$CHO

H$_2$CO(3) - NH$_2$CHO
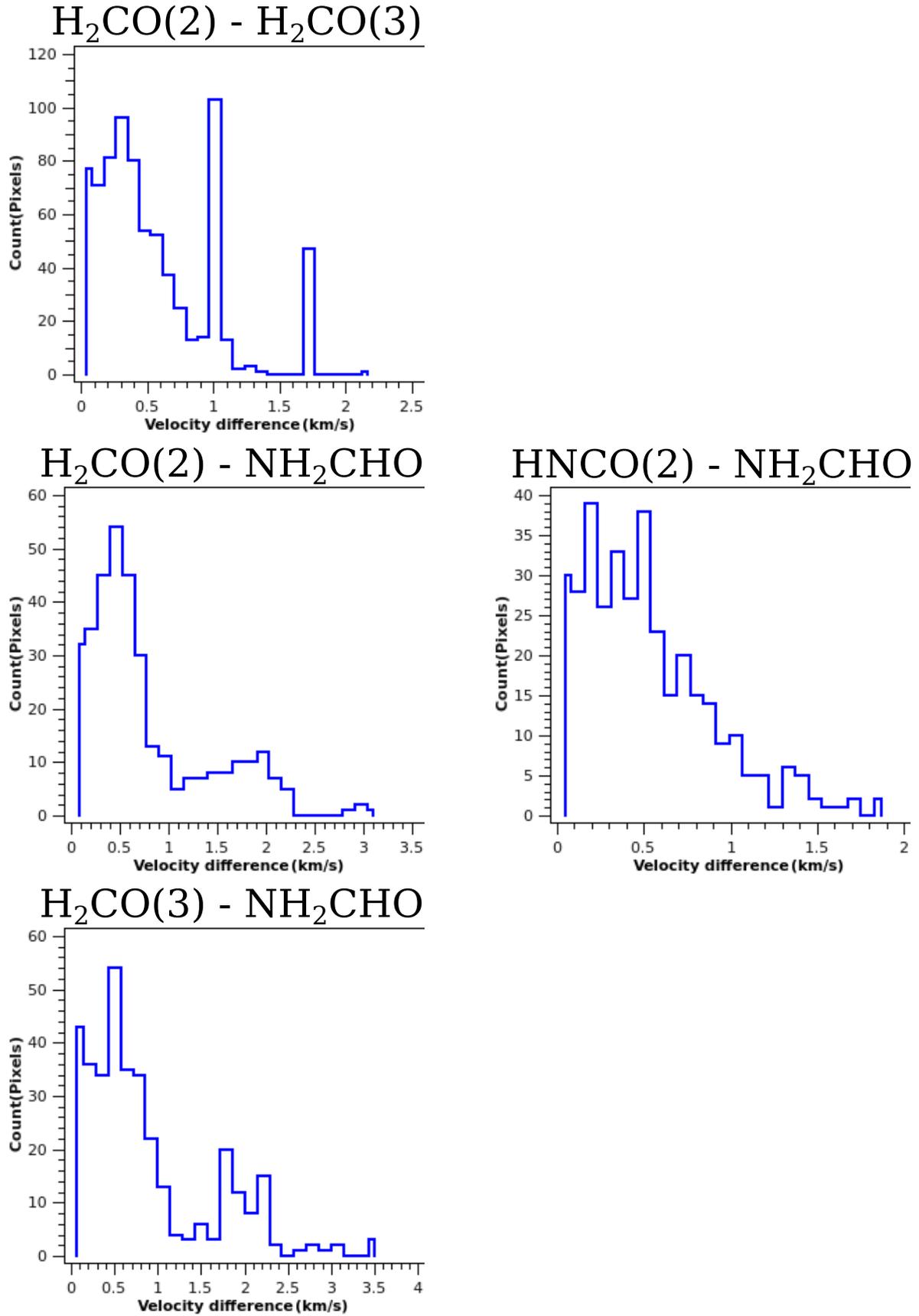
Fig. C.5. G345 Main first moment difference histogram.

H$_2$CO(2) - H$_2$CO(3)

HNCO(2) - HNCO(3)

H$_2$CO(2) - NH$_2$CHO

HNCO(2) - NH$_2$CHO

H$_2$CO(3) - NH$_2$CHO

HNCO(3) - NH$_2$CHO
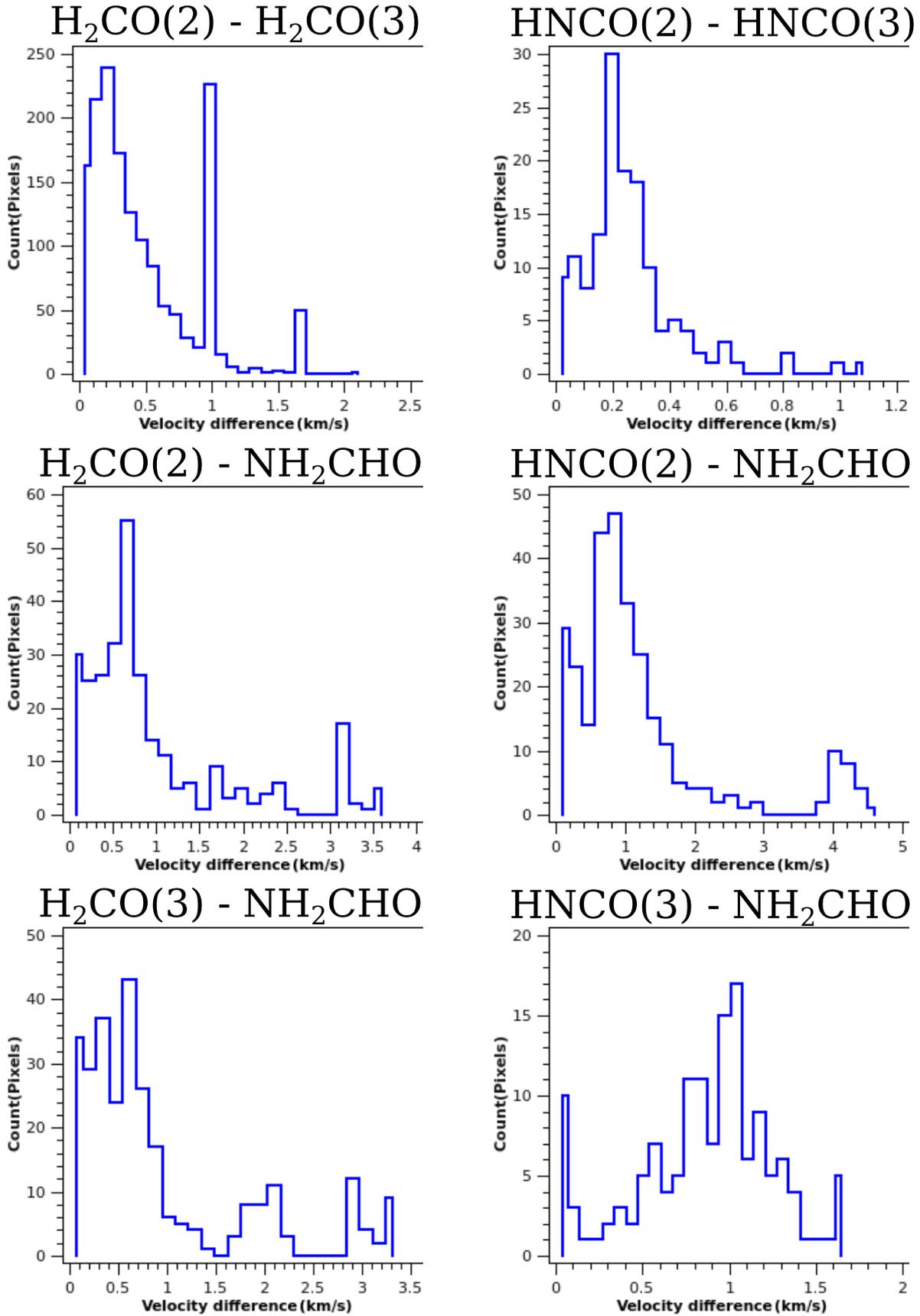
Fig. C.6. G345 NW spur first moment difference histogram.

H₂CO(2) - H₂CO(3)

H₂CO(2) - NH₂CHO

HNCO(2) - NH₂CHO

H₂CO(3) - NH₂CHO
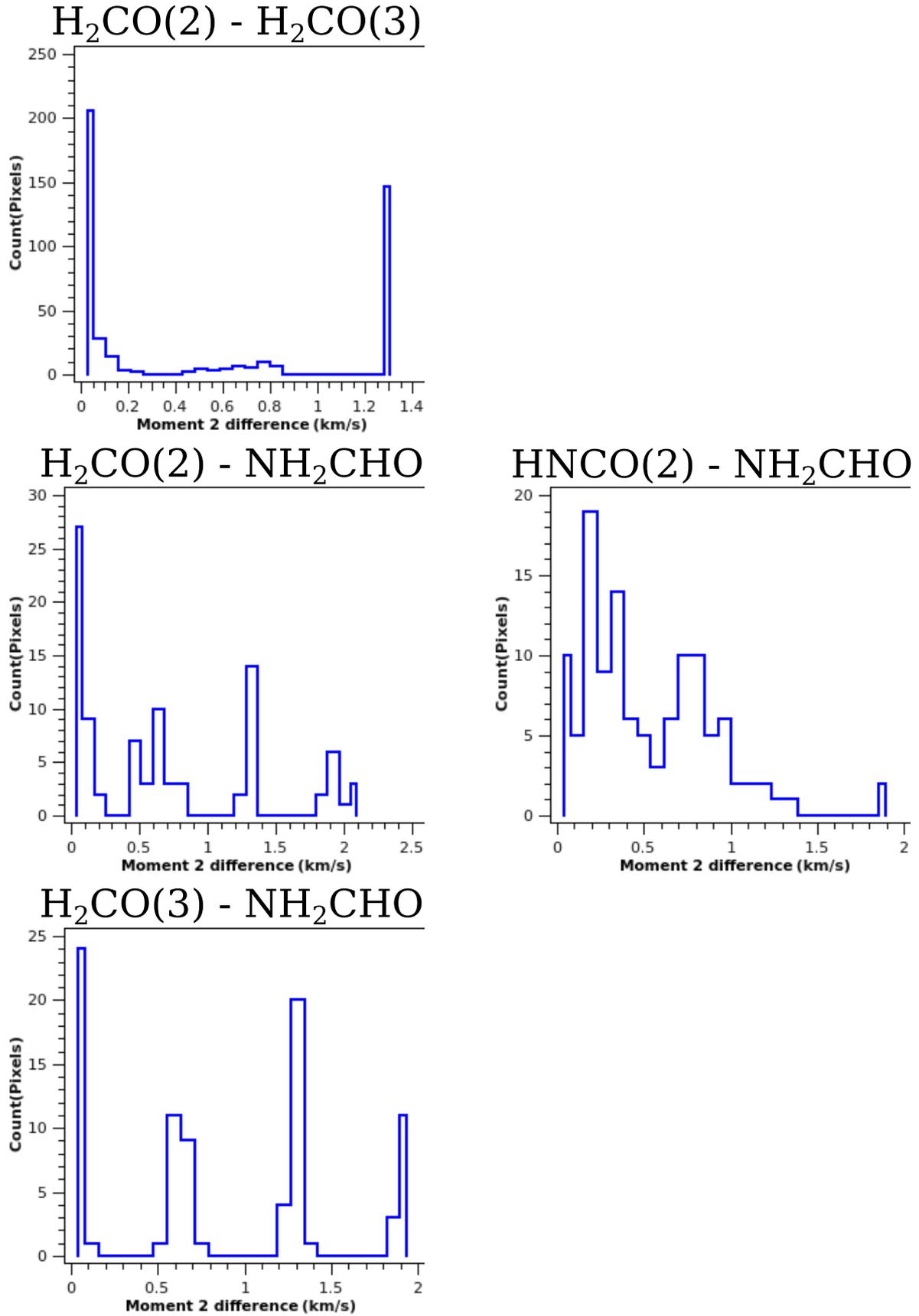
Fig. C.7. G17 second moment difference histogram.

H₂CO(2) - H₂CO(3)

HNCO(3) - HNCO(1)

H₂CO(2) - NH₂CHO

HNCO(1) - NH₂CHO

H₂CO(3) - NH₂CHO

HNCO(3) - NH₂CHO
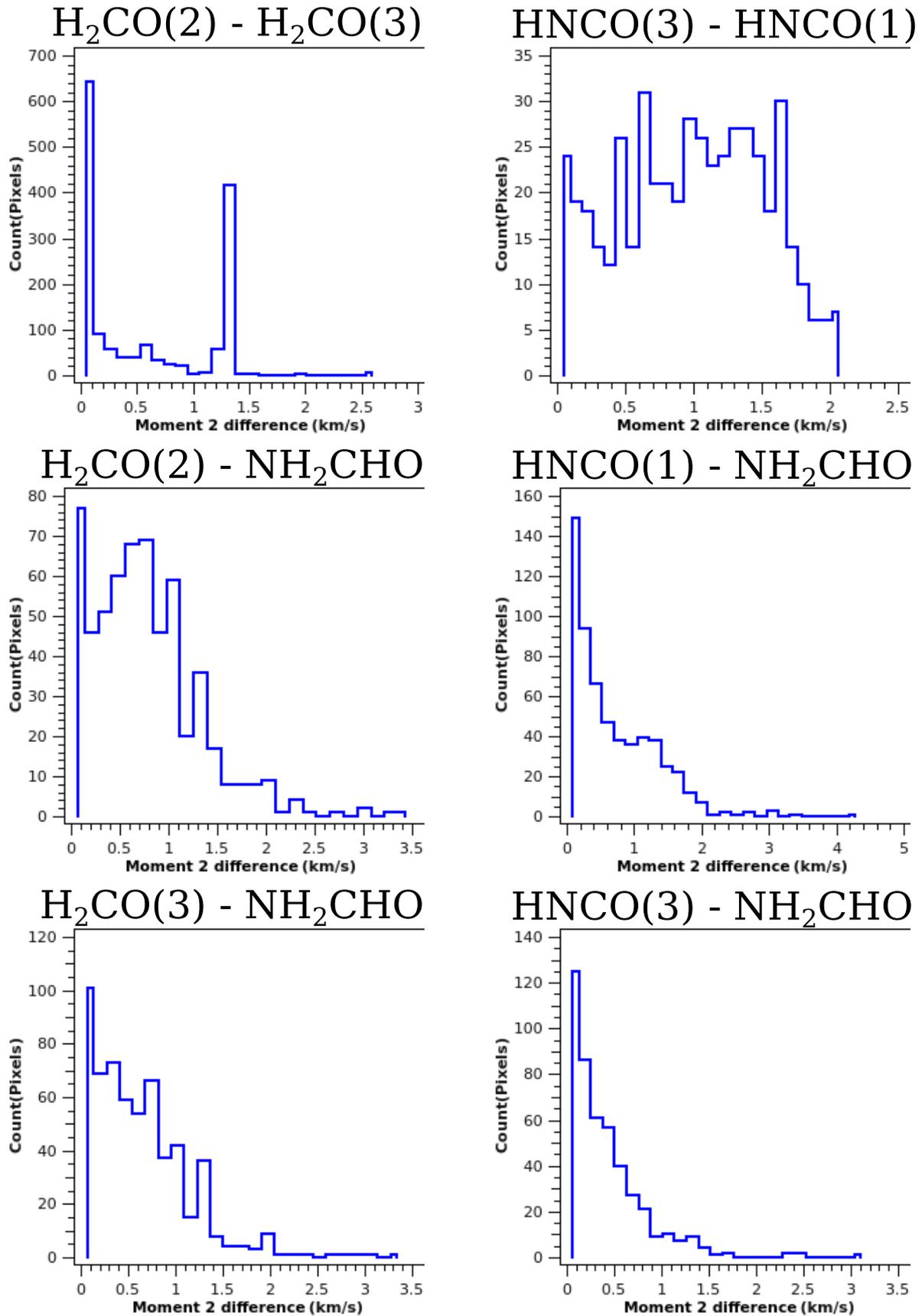
Fig. C.8. G24A1 second moment difference histogram.

H$_2$CO(2) - H$_2$CO(3)

HNCO(3) - HNCO(1)

H$_2$CO(2) - NH$_2$CHO

HNCO(1) - NH$_2$CHO

H$_2$CO(3) - NH$_2$CHO

HNCO(3) - NH$_2$CHO
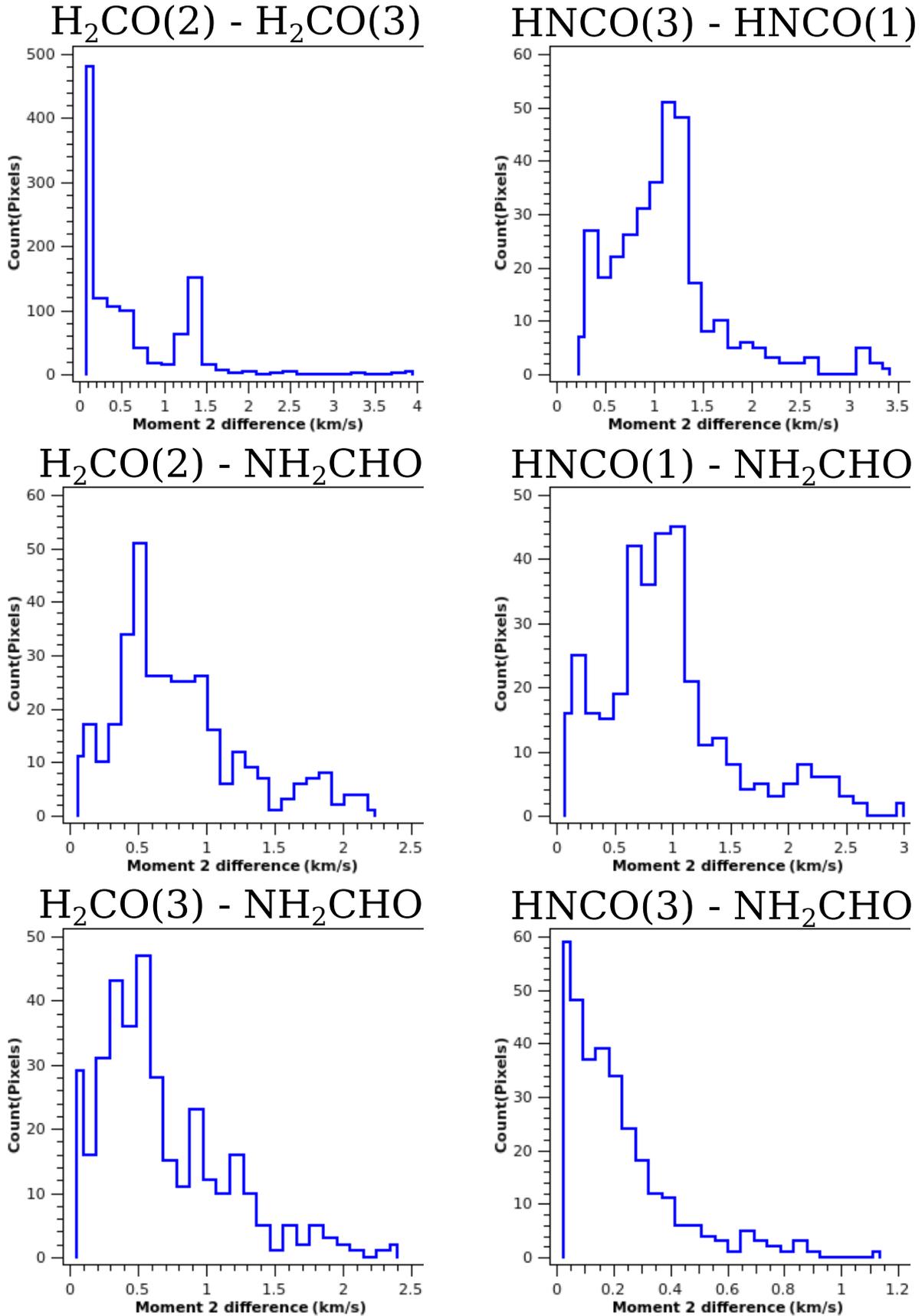
Fig. C.9. G24A2(N) second moment difference histogram.
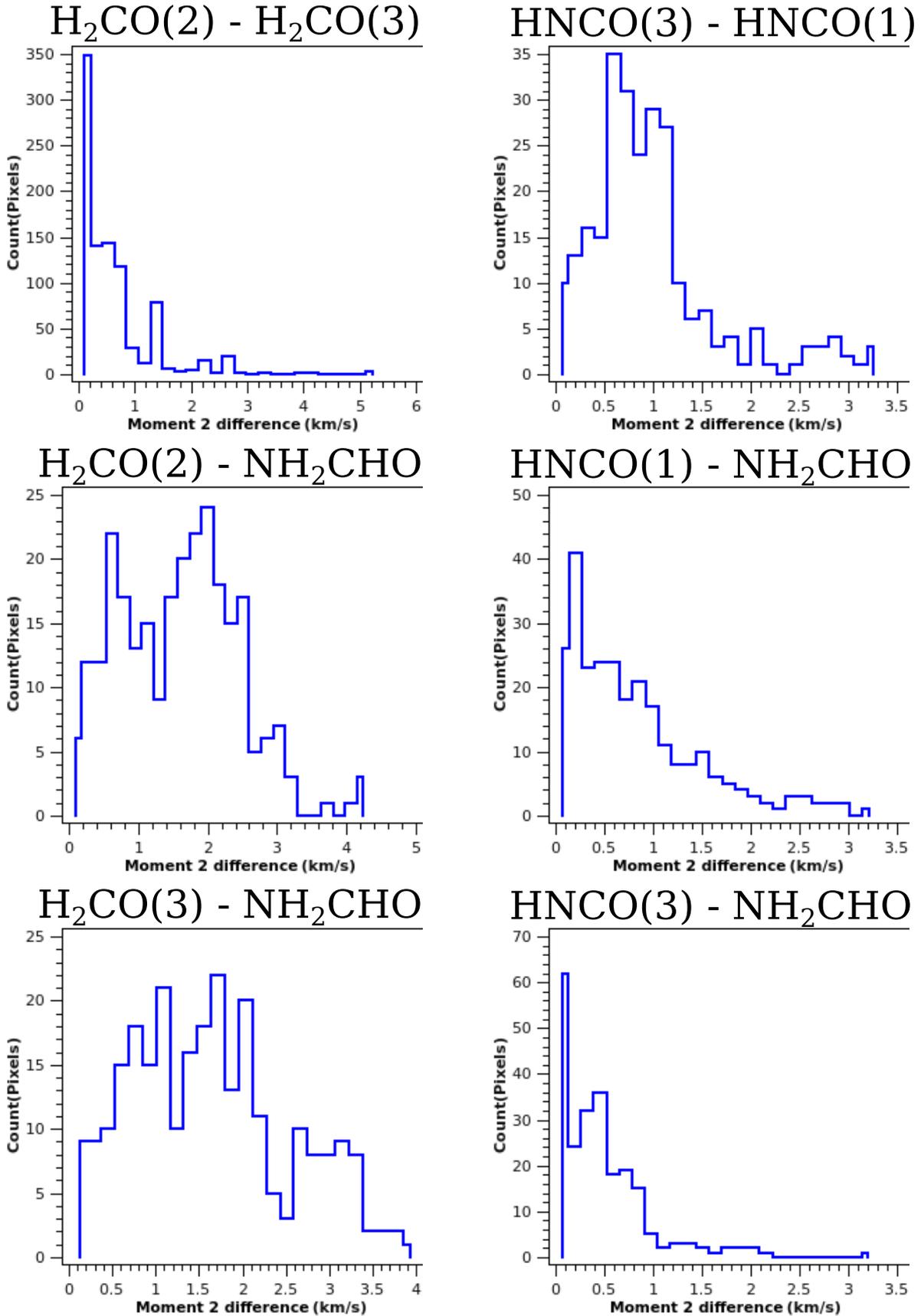
**Fig. C.10.** G24A2(S) second moment difference histogram.
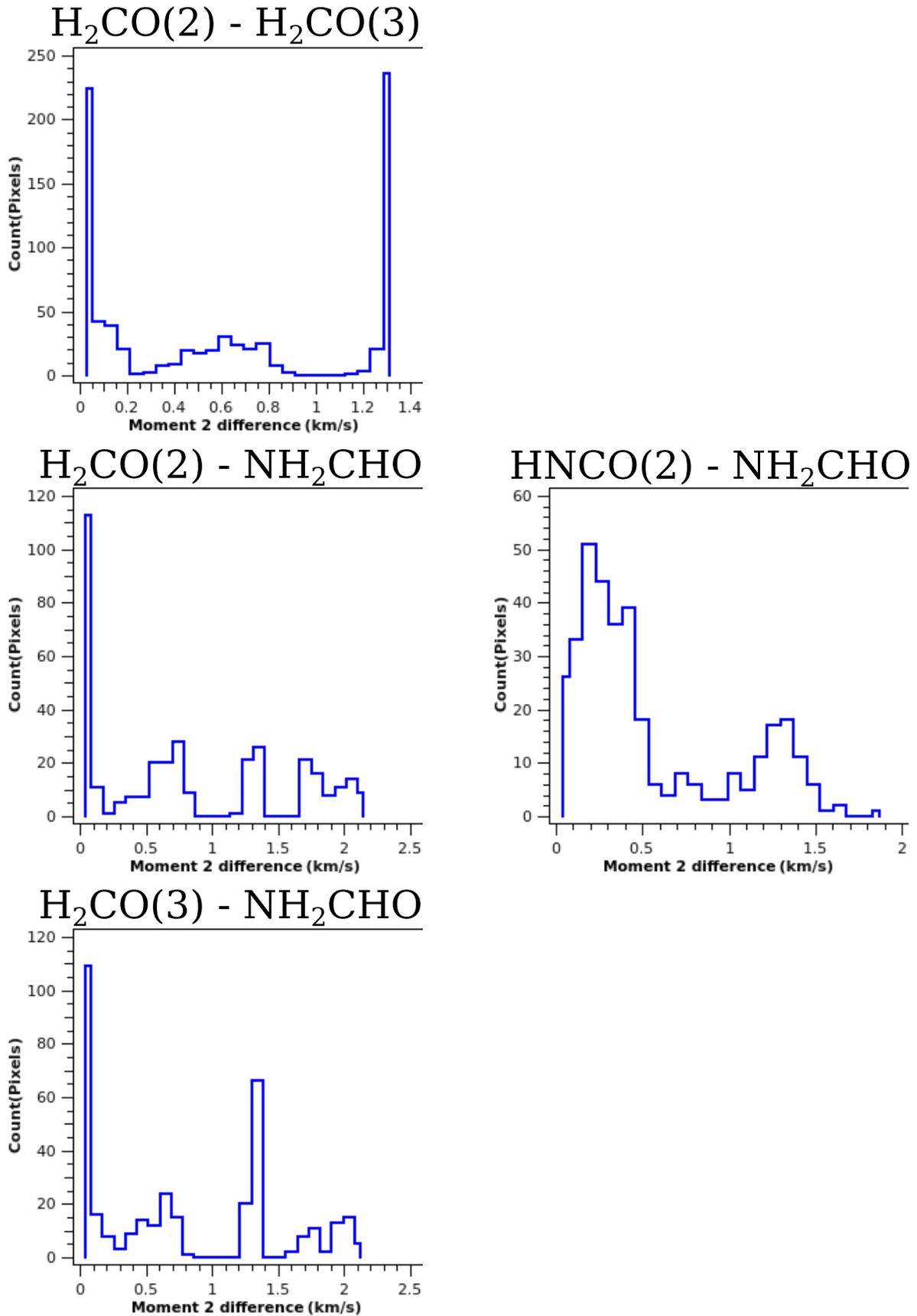
Fig. C.11. G345 Main second moment difference histogram.
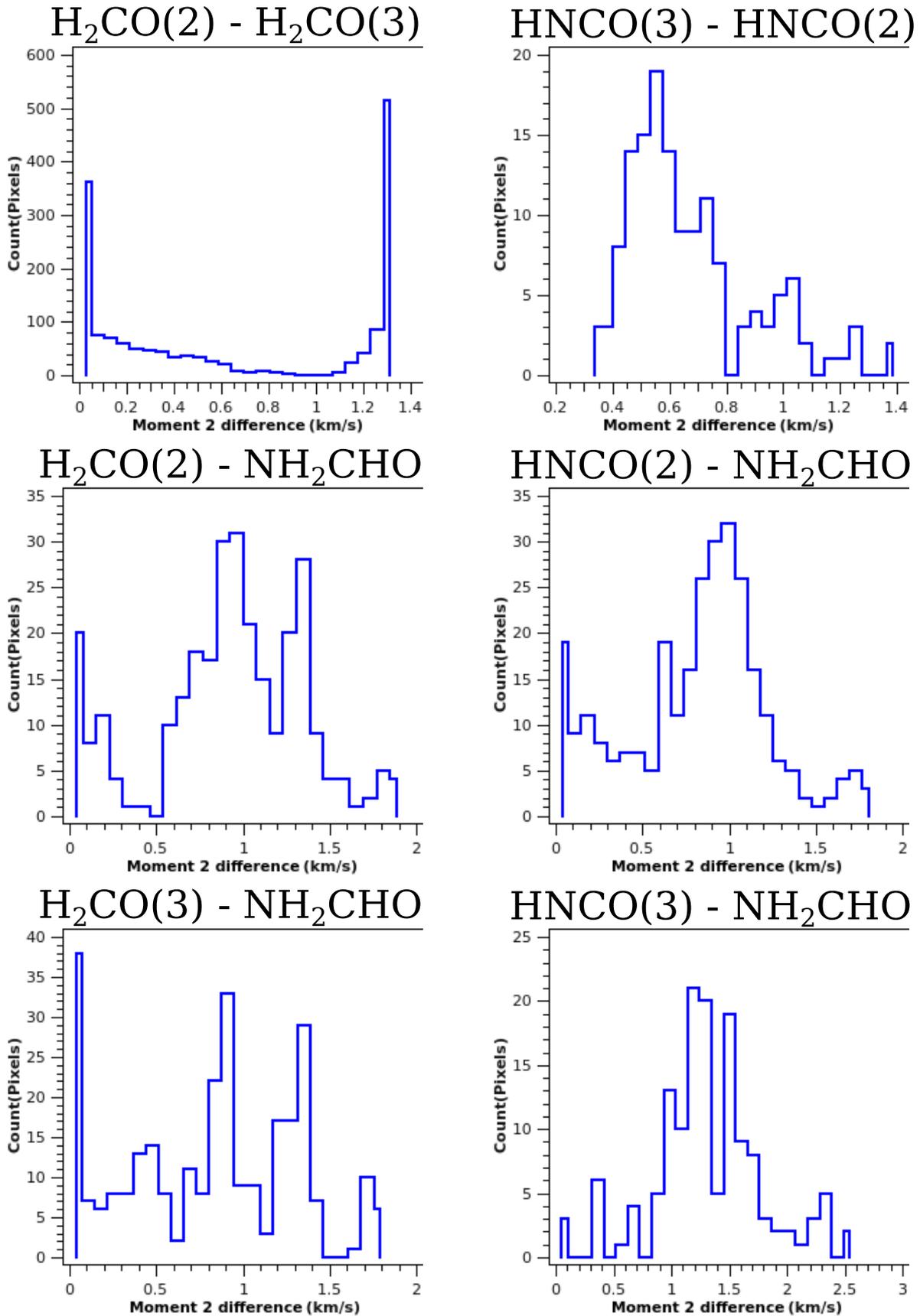
Fig. C.12. G345 NW spur second moment difference histogram.